DEPARTMENT OF THE INTERIOR
U.S. GEOLOGICAL SURVEY

FAULTS, FRACTURES, AND OTHER DEFORMATION FEATURES PRODUCED DURING LOADING OF GRANITE IN TRIAXIAL EQUIPMENT

By
D.E. Moore, R. Summers, and J.D. Byerlee

Open-File Report 90-349

This report is preliminary and has not been reviewed for conformity with U.S. Geological Survey editorial standards or with the North American Stratigraphic Code. Any use of trade, product or firm names is for descriptive purposes only and does not imply endorsement by the U.S. Government.

Menlo Park, CA 94025
1990

ABSTRACT

Maps are presented of the fractures and faults that developed in originally intact cylinders of granite during triaxial experiments at room temperature. Additional deformation features are described graphically. With increasing axial compression prior to sample failure, the samples show increases in the numbers of microfractures, kinked micas, and flame-perthite-bearing feldspars; the latter feature is an exsolution/replacement texture in K-feldspar whose development is commonly attributed to the application of a differential stress. The overall pattern of fracturing following sample failure varies from sample to sample, but the orientation of the main fault in a given sample can be correlated with the confining pressure of the experiment. Interpretive maps of the paths of concentrated shear show that shearing is much more localized during stick-slip motion than during stable sliding. Localization of shear accompanying stick slip has also been observed following friction experiments in which the samples contained a layer of artificial or natural gouge placed along a sawcut. These similar results suggest that the deformation textures reflect the processes controlling the sliding behavior.

INTRODUCTION

In order to study the initiation and development of fault zones and the relationships between fault structures and sliding behavior, we have run a series of triaxial friction experiments using originally intact cylinders of granite. To aid in the investigation, maps were prepared of the fracture patterns and the zones of concentrated shear that were visible in thin sections of the samples. Preliminary results of this study are presented in Moore et al. (1990). Because of space limitations, only selected fault maps could be included in that paper. The main purpose of this report is to present all of the deformation maps, to serve as a data base for Moore et al. (1990) and for any future papers on this topic. Measurements made of some additional deformation features observable in thin section, namely kink bands and flame perthite, are included at the end of this report.

STARTING MATERIALS

The experiments were run using intact cylinders of Westerly and Barre granite, both of which rock types have been extensively employed in geophysical studies. They are typically referred to as granites in the rock mechanics literature and will be called granites in this paper as well. However, both rocks classify as granodiorites based on their mineral proportions (Moore et al., 1987); principally, this means that Barre and Westerly contain considerably less K-feldspar and more plagioclase than a true granite. The two rock types have very similar primary and secondary mineral assemblages, but they differ somewhat in their textures, as illustrated in Figure 1. The mineral assemblages and mineral compositions of Westerly and

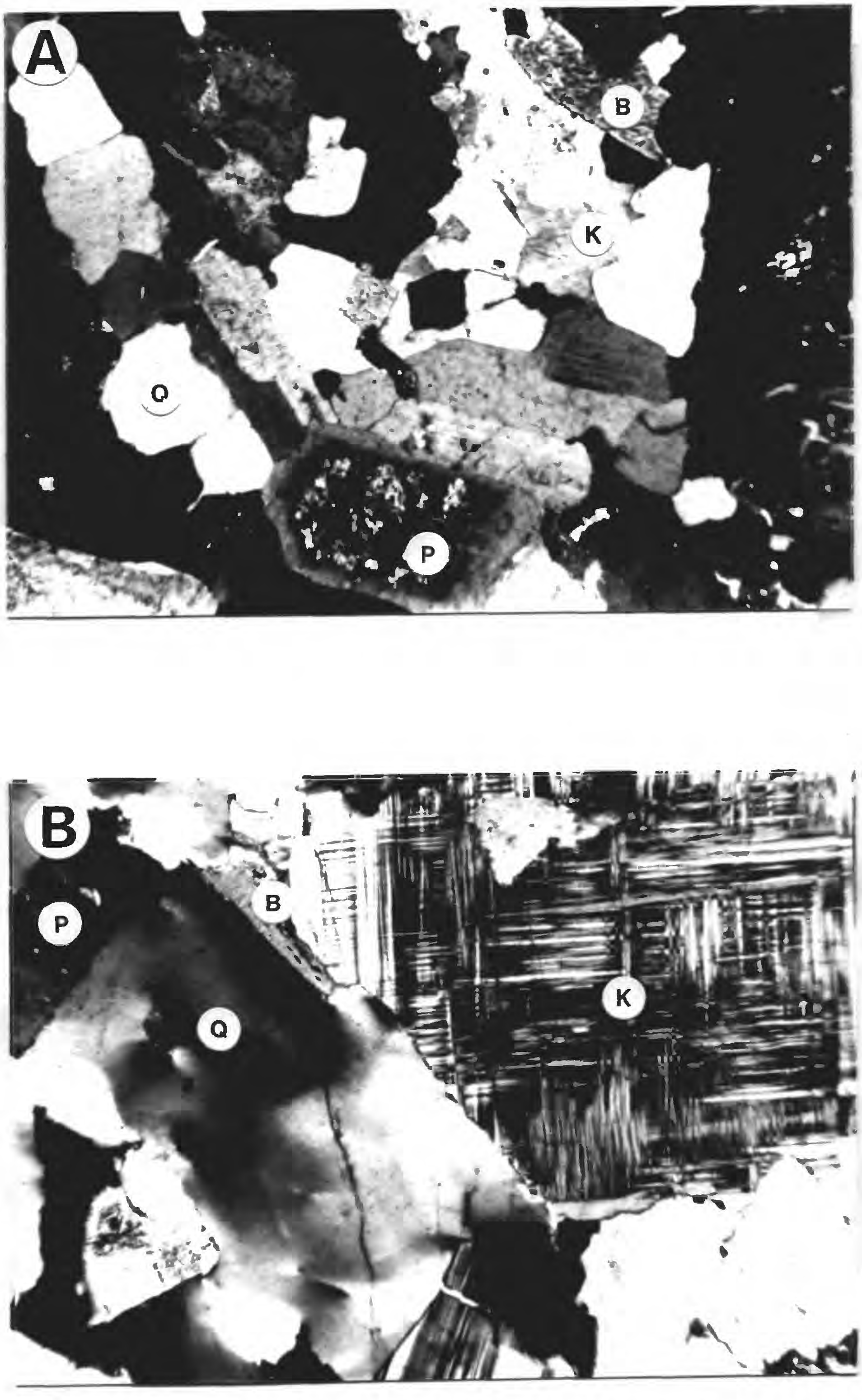

Figure 1. Photomicrographs of a) Westerly and b) Barre starting materials. Westerly is medium-grained, relatively uniform-looking and essentially undeformed. Barre is considerably coarser grained, particularly with respect to quartz and K-feldspar, and also somewhat deformed, as indicated in b) by the strained quartz phenocryst and elsewhere by kinked micas and aligned fractures. Note the long, intragranular fracture in the quartz phenocryst in b).

Barre are described in Moore et al. (1987); of principal interest to this study are their textural characteristics, which are described briefly below.

The Westerly samples are medium-grained and have a uniform appearance (Fig. 1a). They consist of subhedral plagioclase crystals up to 2.2 mm long and somewhat smaller (about 1 mm diameter) anhedral quartz and anhedral to subhedral K-feldspar crystals. Mafic minerals, including biotite which averages 0.35 mm in its longest dimension with a maximum of 1.5 mm, are evenly distributed throughout the rock. The Westerly samples are not foliated, and neither the quartz nor the feldspar crystals are highly strained. Some of the crystals, particularly quartz, do contain intragranular and grain-boundary fractures; an example of such fractures that are filled with fine-grained muscovite is shown in Figure 9 of Moore et al. (1987, p. 20).

The Barre samples (Fig. 1b) are coarser grained than the Westerly ones (Fig. 1a), and they are dominated by anhedral and highly strained quartz and K-feldspar crystals, up to 3.5 mm long, which wrap around smaller (0.8 to 1 mm diameter) crystals of plagioclase, quartz, and mafic minerals. The biotites in the Barre samples are also coarser grained than their counterparts in Westerly, averaging 0.6 mm in their longest dimension with a maximum of about 2 mm. The Barre starting material contains a more extensive array of fractures than Westerly; the fractures are principally intragranular ones within quartz and, to a lesser extent, feldspar. Because of the larger maximum grain size of Barre, its intragranular fractures also tend to be longer than those found in the Westerly samples. Many of the fractures in Barre have approximately the same trend, which imparts a mild fabric to the rock when viewed in thin section. Some of these fractures are filled with calcite, muscovite, or other secondary minerals.

EXPERIMENTS CONDUCTED

The experiments can conveniently be divided into 3 groups that were conducted at different times. The experimental conditions for the 3 groups of samples are summarized in Table 1. All of the experiments were run at room temperature; Groups I and III use Westerly cylinders and Group II uses Barre. Group I is derived from an older set of experiments whose strength data are reported in Summers and Byerlee (1977); the deformation textures developed in these samples have not previously been described.

The granite cylinders were approximately 25 mm in diameter and 65 mm in length. All of the Westerly experiments were conducted on room-dry samples, whereas all but two of the Barre experiments used cylinders that had been pre-saturated with deionized water (Table 1). No externally controlled pore pressure was applied during any of the experiments. The Westerly experiments of Group I are separable into two sets that were run at different rates of axial loading; the experiments of Groups II and III were run at the slower of the two Group I strain rates. The main variable in the experiments was the confining pressure; because the sliding behavior is a function of the confining pressure, a wide range of pressures was tested to provide several examples each of stick-slip and stable motion for textural comparison.

All of the Group I experiments were run until the jackets failed; with a single exception, this involved several millimeters of shear along the generated fault surface. Two of the Group II and four of the Group III experiments were stopped just after the failure point of the sample;

Table 1. EXPERIMENTS CONDUCTED

	Pc(MPa)	Axial loading rate (mm/sec)	Dry/Fluid saturated	Comments
Group I				
Westerly				
W1a	41	.00635	Dry	Stable slip
W2a	83	.00635	Dry	Stable slip
W3a	120	.00635	Dry	Stable slip
RSW1	277	.00635	Dry	Stick slip
R90	621	.00635	Dry	Stick slip
R91	313	.00635	Dry	Stick slip
W2b	78	.000635	Dry	Stable slip
W3b	118	.000635	Dry	Stable slip
R120	389	.000635	Dry	Stick slip
R122	486	.000635	Dry	To failure
R123	485	.000635	Dry	Stick slip
R125	585	.000635	Dry	Stick slip
Group II				
Barre				
RSG1B	485	.000635	Dry	To 90% failure
RSG2B	485	.000635	Dry	To 67% failure
RSG3B	50	.000635	Sat.	Stable slip
RSG4B	100	.000635	Sat.	Stable slip
RSG5B	200	.000635	Sat.	Mostly stick slip
RSG6B	300	.000635	Sat.	Stick slip
RSG7B	400	.000635	Sat.	Stick slip
RSG8B	500	.000635	Sat.	Stick slip
RSG9B	100	.000635	Sat.	To failure
RSG10B	500	.000635	Sat.	To failure
RSG11B	500	.000635	Sat.	To 90% failure
RSG12B	500	.000635	Sat.	To 67% failure
Group III				
Westerly				
RSG501	100	.000635	Dry	To failure
RSG502	100	.000635	Dry	To failure
RSG503	100	.000635	Dry	To 99% failure
RSG504	100	.000635	Dry	To 90% failure
RSG505	500	.000635	Dry	To failure
RSG506	500	.000635	Dry	To failure
RSG507	500	.000635	Dry	To 99% failure
RSG508	500	.000635	Dry	To 90% failure

these experiments are useful for separating the textural effects of the initial break from those superimposed during shear. Four experiments each of Groups II and III were halted prior to sample failure, at some percentage of the failure stress as determined from previous runs that went beyond the failure point. These latter experiments were conducted to study the development of deformation features such as microfracturing and kink bands in the cylinders prior to sample failure.

STRENGTH AND SLIDING BEHAVIOR

Plots of differential stress versus axial compression for Groups I and II of Table 1 are presented in Figures 2-5; only those experiments are shown for which sliding was continued after the initial break. All of the experiments of Group III were terminated either immediately before or after the initial failure, and the strength plots for that group are not included in this report. The results for Westerly granite in Figures 2 and 3 are taken from Summers and Byerlee (1977); their report also contains additional strength data from intact-rock experiments on Westerly.

With increasing confining pressure there is a corresponding increase in the stresses supported both at the initial failure point and during the subsequent frictional sliding of the samples. The sliding behavior also changes from stable slip at low confining pressures to stick-slip motion at high confining pressures. The Barre sample at 200 MPa (Fig. 4) displays transitional sliding behavior, with an early period of stable slip followed almost completely by stick-slip motion. No Group I Westerly experiment (Figs. 2 and 3) was conducted at a confining pressure near 200 MPa; however, transitional behavior was observed in several other intact-rock experiments on Westerly granite that were run at confining pressures between 150 and 200 MPa (Summers and Byerlee, 1977). Otherwise comparable Westerly experiments run at different rates of axial loading showed no obvious differences in either strength or sliding behavior (Figs. 2 and 3; this is also better displayed in the larger data set of Summers and Byerlee, 1977).

The faulted Westerly and Barre samples of Groups I and II have similar frictional strengths; however, the failure point occurs at a higher differential stress for Westerly than for Barre (Figs. 2-5). The Group III Westerly samples failed at a differential stress of about 770 MPa in the experiments at 100 MPa confining pressure and at a differential stress of about 1610 MPa in the experiments at 500 MPa confining pressure. These failure strengths are consistent with those shown for Westerly granite in Figures 2 and 3. The more highly strained character of the Barre samples, including the presence of numerous aligned fractures, may have contributed to their decreased failure strengths.

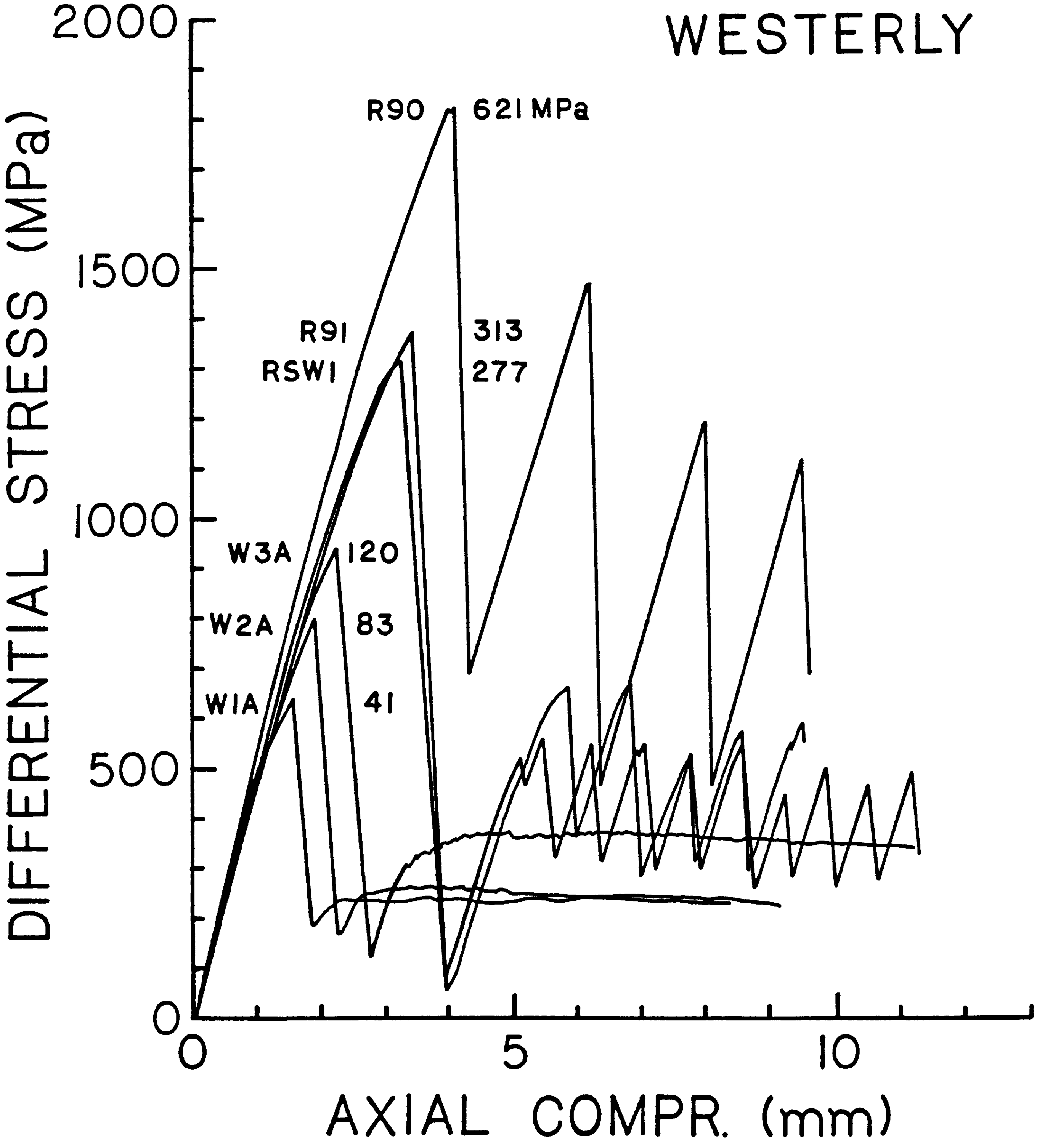

Figure 2. Plot of differential stress versus axial compression for Group I Westerly experiments run at an axial loading rate of 0.00635 mm/sec on room-dry, room-temperature samples. The confining pressure of each experiment is shown across from the sample number.

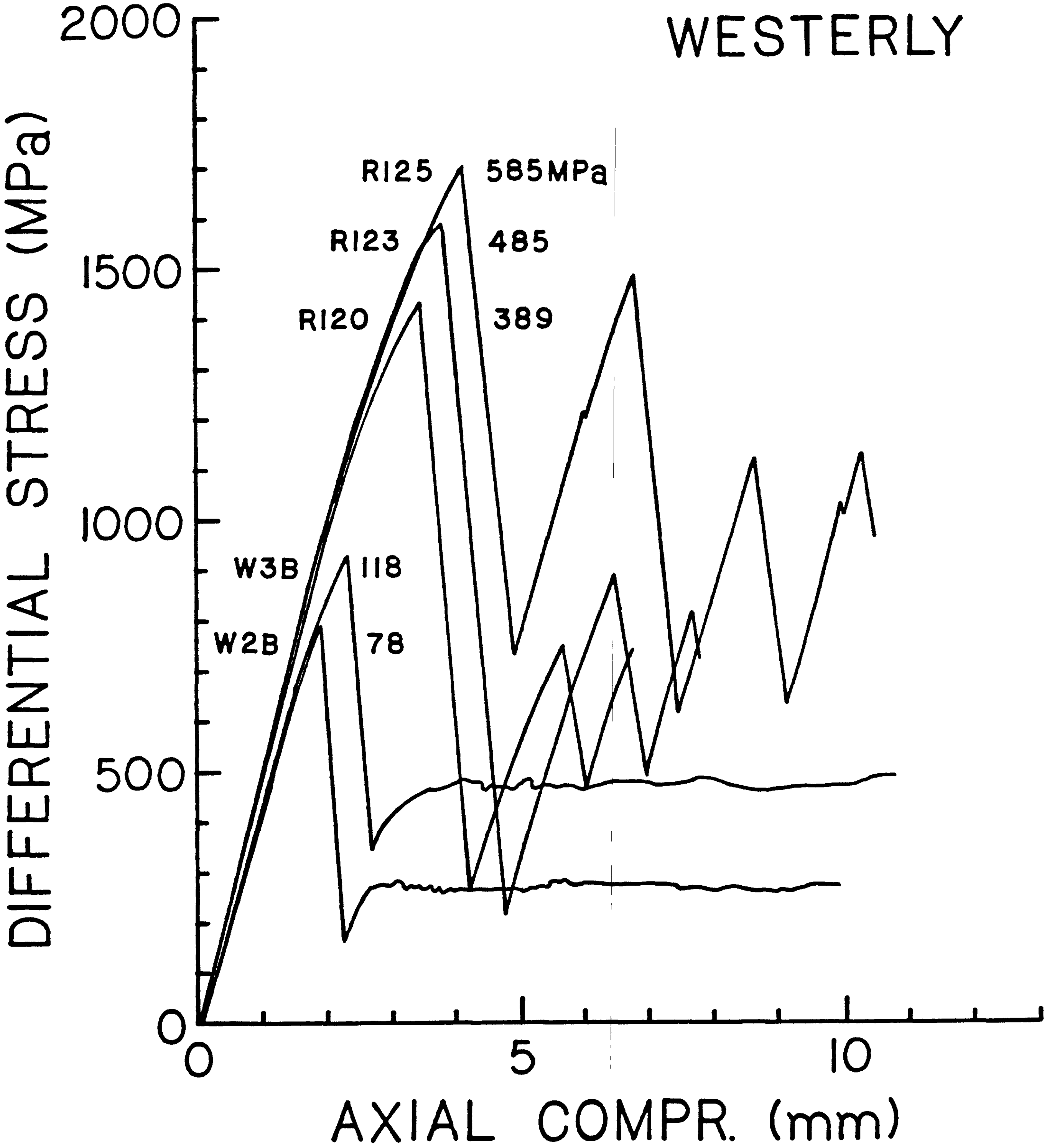

Figure 3. Strength data for Group I Westerly experiments run at 0.000635 mm/sec axial loading rate on room-dry, room-temperature samples. Confining pressures are listed beside the sample numbers.

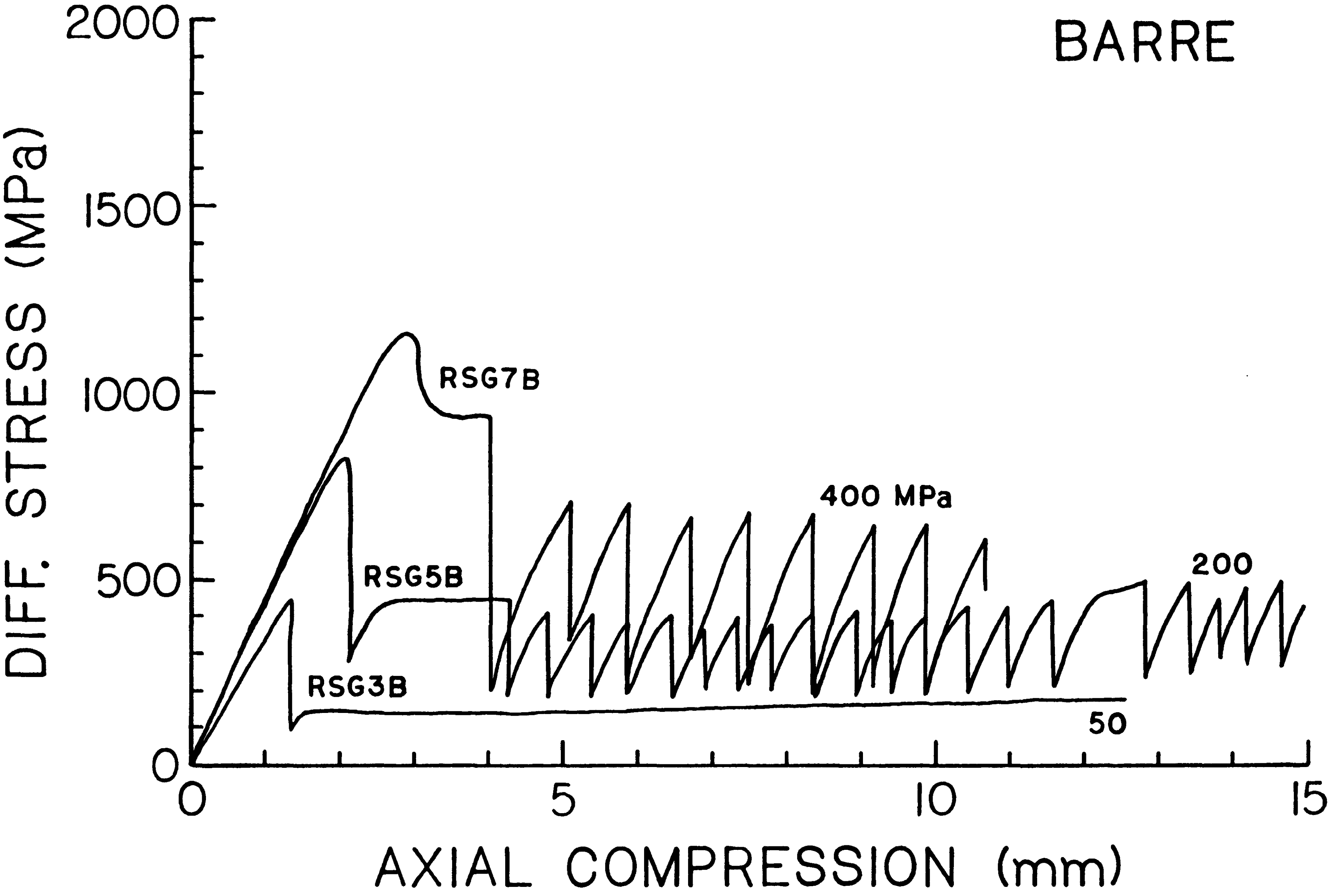

Figure 4. Plot of differential stress versus axial compression for Group II Barre experiments at 50, 200, and 400 MPa confining pressure. The experiments were conducted at room temperature on fluid-saturated samples at an axial loading rate of 0.000635 mm/sec.

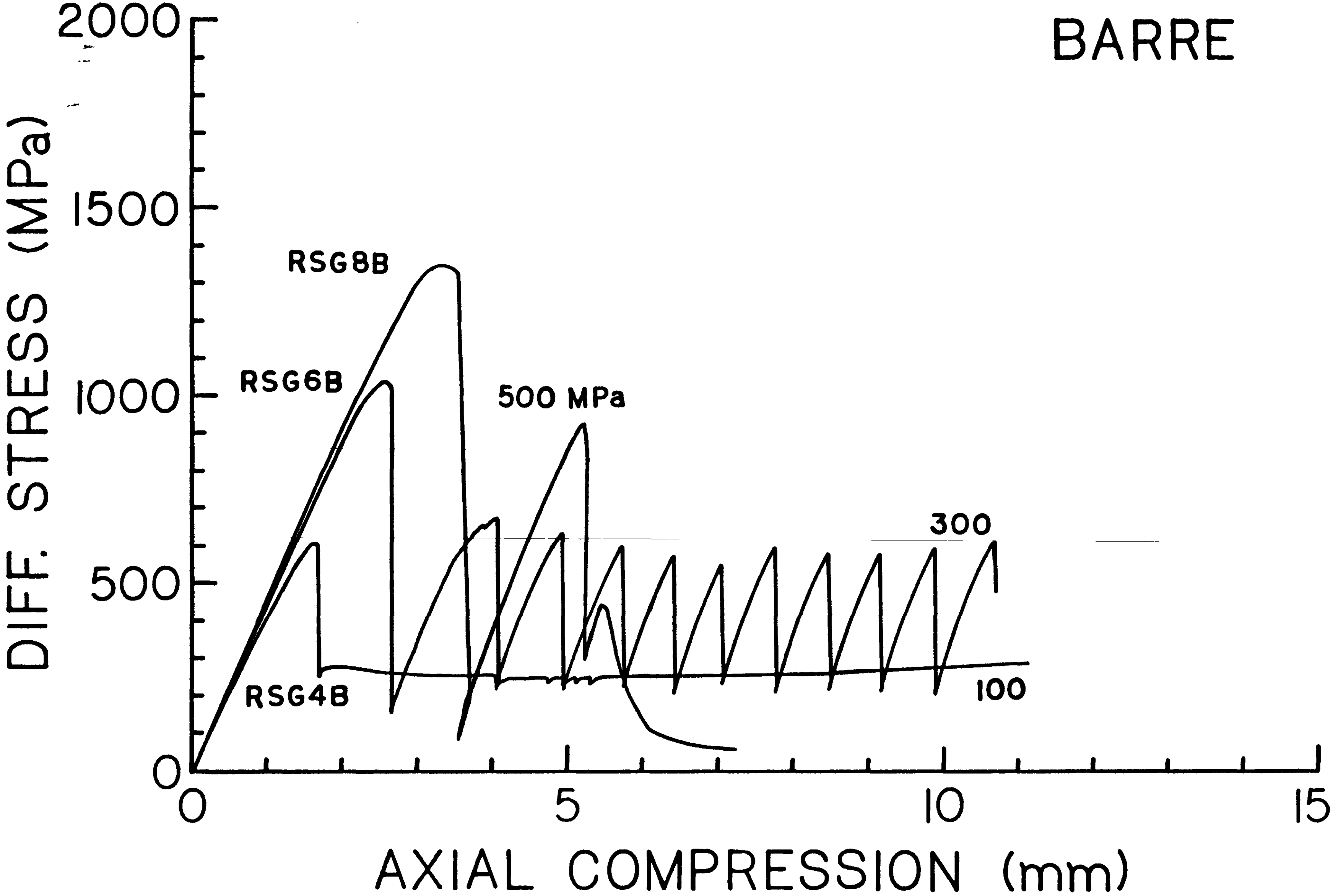

Figure 5. Strength data for Group II Barre experiments at 100, 300, and 500 MPa confining pressure. The experiments were conducted on fluid-saturated samples at room temperature and an axial loading rate of 0.000635 mm/sec.

DEFORMATION MAPS

Thin sections of all the samples listed in Table 1 were examined; the sections were cut parallel to the long axis of the cylinder and, for the faulted samples, perpendicular to the plane of the principal fault zone. The standard-sized sections cover the entire diameter but not the entire length of each granite cylinder. In most cases, the principal fault zone is completely contained in the thin section; the few exceptions are from samples in which the fault plane is oriented at a relatively low angle to the length of the granite cylinder. In order to obtain an overall picture of the deformation textures in the samples, fault/fracture maps of the thin sections were prepared with the aid of a mechanical stage. Examples of the Westerly and Barre starting material were mapped as controls. The results are shown in Figures 6-40. The fractures and faults were mapped on graph paper at a scale of 1" = 5mm; the sample was traversed at 0.5-mm intervals. Two maps were prepared for each of the faulted samples: map a) of each pair shows the major fractures in the sample, and map b) delineates the paths along which shearing appears to have been concentrated. The criteria used to identify the shear paths were based on textures observed in previous studies of shearing in layers of gouge (Moore et al., 1986, 1988, 1989) and included the offset of minerals along fractures, a reduction in grain size, the development of a foliation, and the formation of secondary shear bands. Photomicrographs of some of these textural features are presented in Moore et al. (1990, Figs. 4 and 5).

The three groups of samples were mapped at different degrees of detail. The cut-off length for mapping fractures in the Group I and II samples was about 0.5 mm (although some shorter fractures that are closely associated with longer ones were included). This minimum led to the exclusion of many intragranular cracks from the Group I Westerly maps. Because of the larger average grain size in Barre, particularly with respect to quartz, many of the intragranular cracks were long enough to be included in the Group II Barre maps. One of the original purposes of the Group III Westerly experiments was to study the progressive development and orientations of microfracturing as the failure point of the granite was approached; for these maps, therefore, the cut-off fracture length was reduced to about 0.25 mm.

The samples of Group III show that the density of microfracturing increases with increasing axial compression prior to sample failure (Figs. 35, 36, 39, 40). The samples run at 500 MPa confining pressure have a higher density of microfracturing than those run at 100 MPa. Hand specimens of the unfaulted samples such as those shown in Figures 21 and 31 provide no clue to where the fault would have formed, to aid in orienting the thin section. Nevertheless, whatever their orientations, the thin sections obtained from such samples would necessarily intersect the potential fault surface in a diagonal to horizontal line. However, the patterns of microfracturing in those samples run to 90% (Figs. 20, 30, 36, and 40) and even 99% (Figs. 35 and 39) of the failure stress also give no indication of the eventual position of the fault.

The outline of the fault zone obtained from experiments that were halted immediately after the initial failure is generally quite irregular, and the fault consists of a number of large fragments without smooth boundaries. Evidence of shear in such samples is relatively scarce and of scattered distribution, and the resulting maps of the slip paths are a series of short, unconnected lines (e.g., Figs. 28, 33, 34). Following several millimeters of shear, the boundaries of the fault zone are better defined and the slip paths much more continuous; apparent discontinuities in the slip paths of these samples are caused for the most part by erosion of the relatively weak fault-zone material during thin-section preparation. Such gaps produced by the

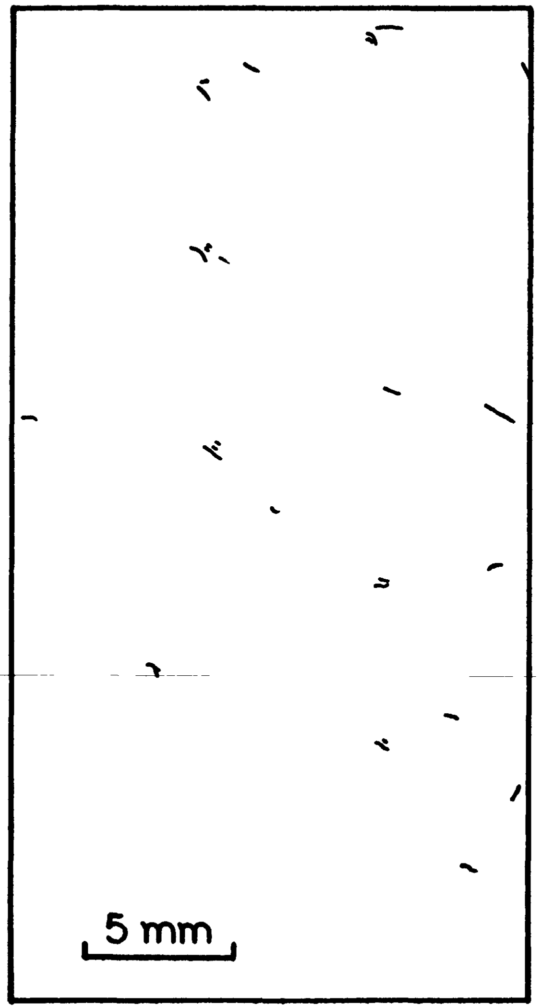

Figure 6. Map of microfractures in a sample of the Group I Westerly starting material. The cut-off length for single fractures in Group I was approximately 0.5 mm, but shorter fractures that occur in clusters with longer ones have been included; a few such clusters are present in this map.

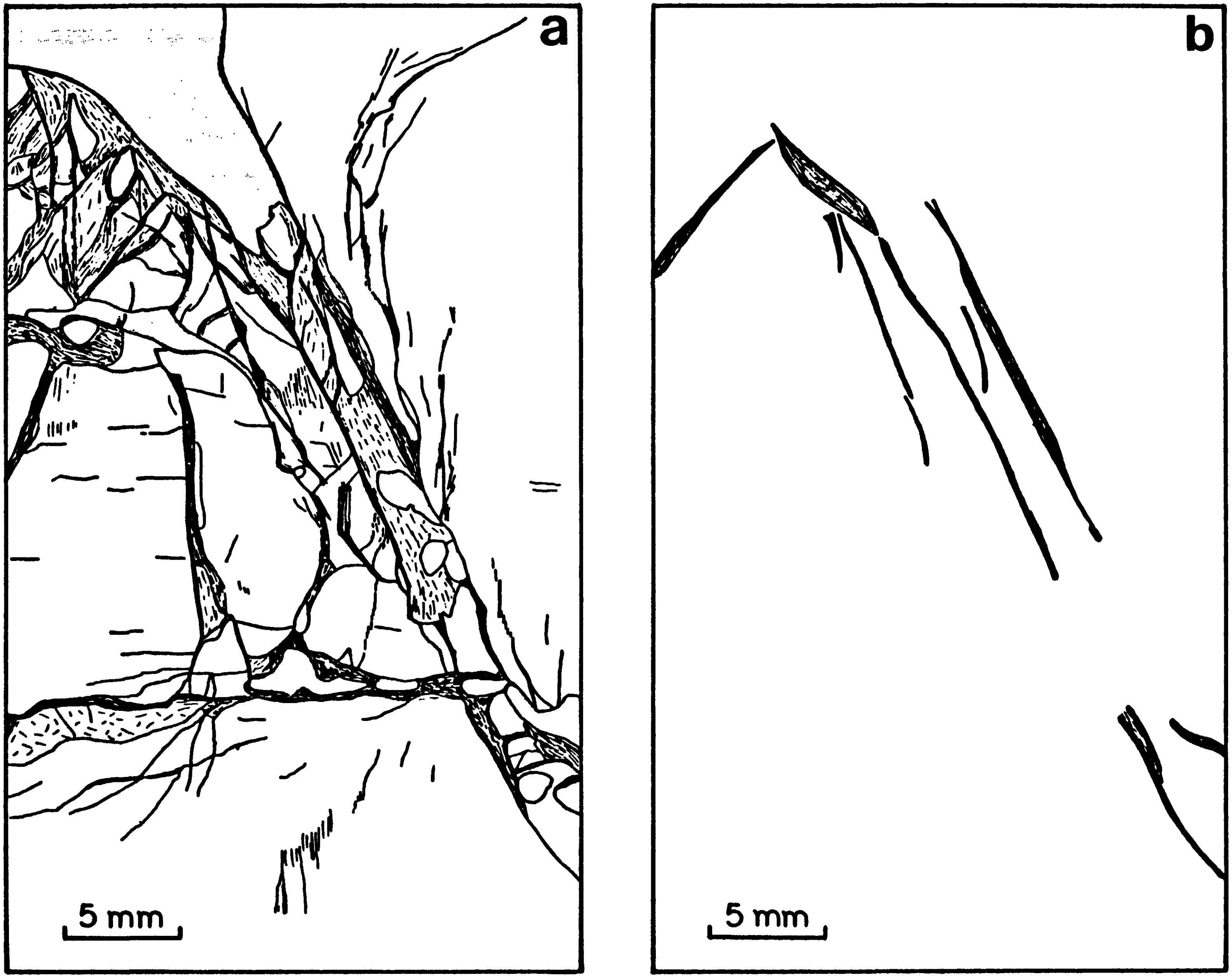

Figure 7. Maps of a) all fractures and b) principal slip paths of Group I sample W1a. The light stippled pattern in this and many other maps, which is prominently shown for example in the upper left corner of a), indicates a gap in the thin section caused by erosion during its preparation. The criteria for shear used to delimit the zones of concentrated slip in b) are described in the text.

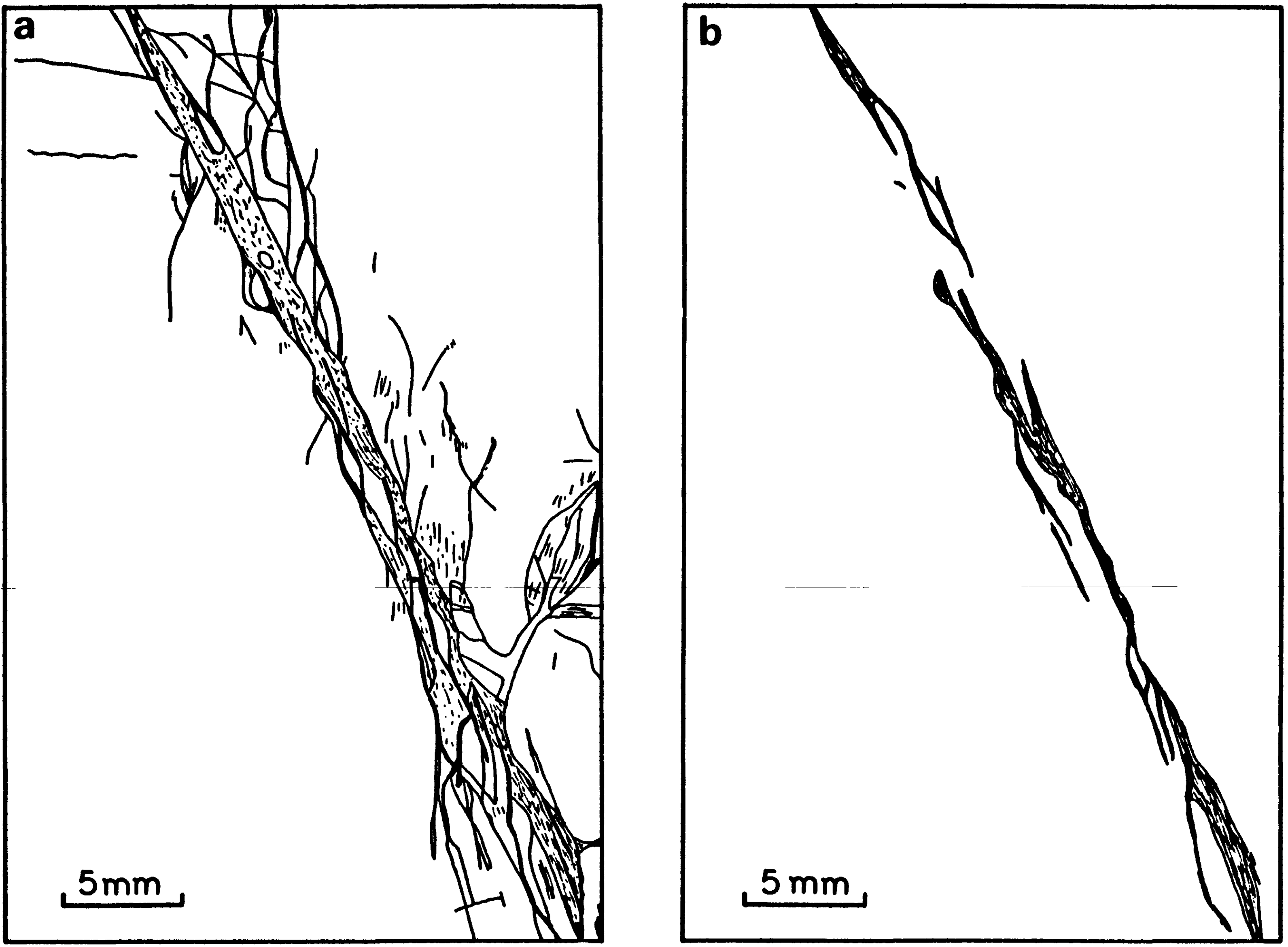

Figure 8. Maps of a) all fractures and b) principal slip apths in Group I sample W2a.

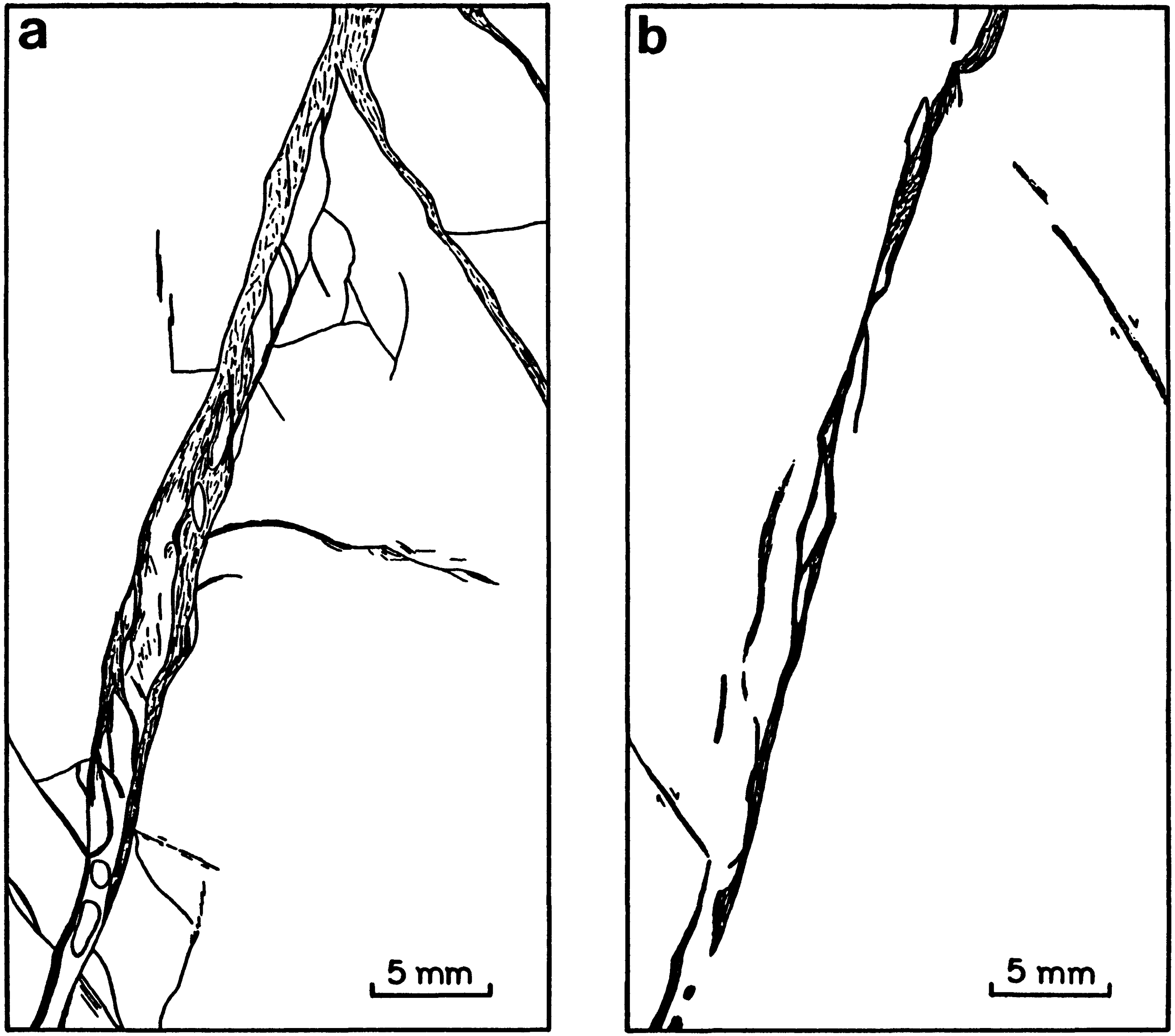

Figure 9. Maps of a) all fractures and b) principal slip paths in Group I sample W3a. The pairs of arrows in the lower left- and upper right-hand corners of b) and also present in some other figures are shear directions determined by offset grains.

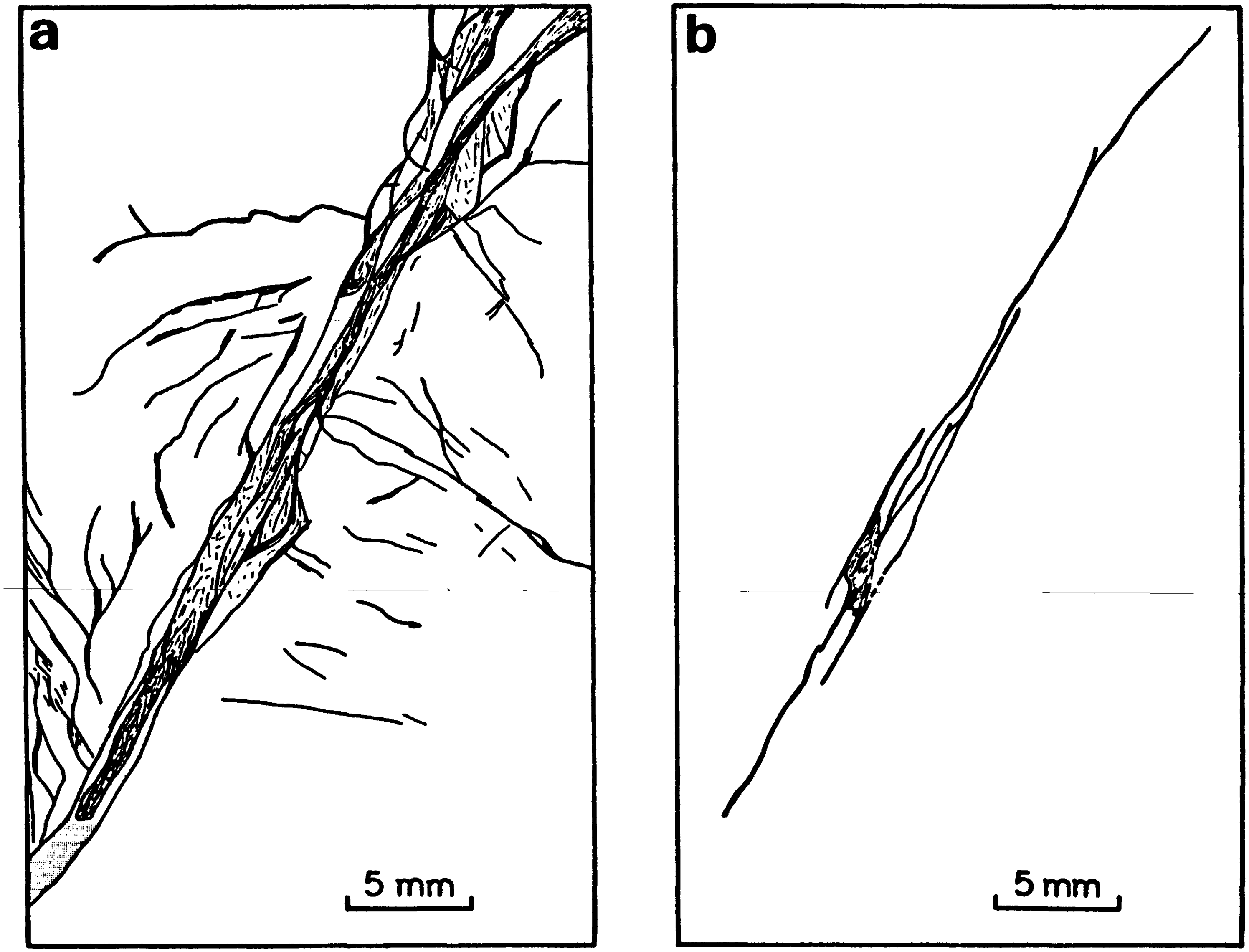

Figure 10. Maps of a) all fractures and b) principal slip paths in Group I sample RSW1.

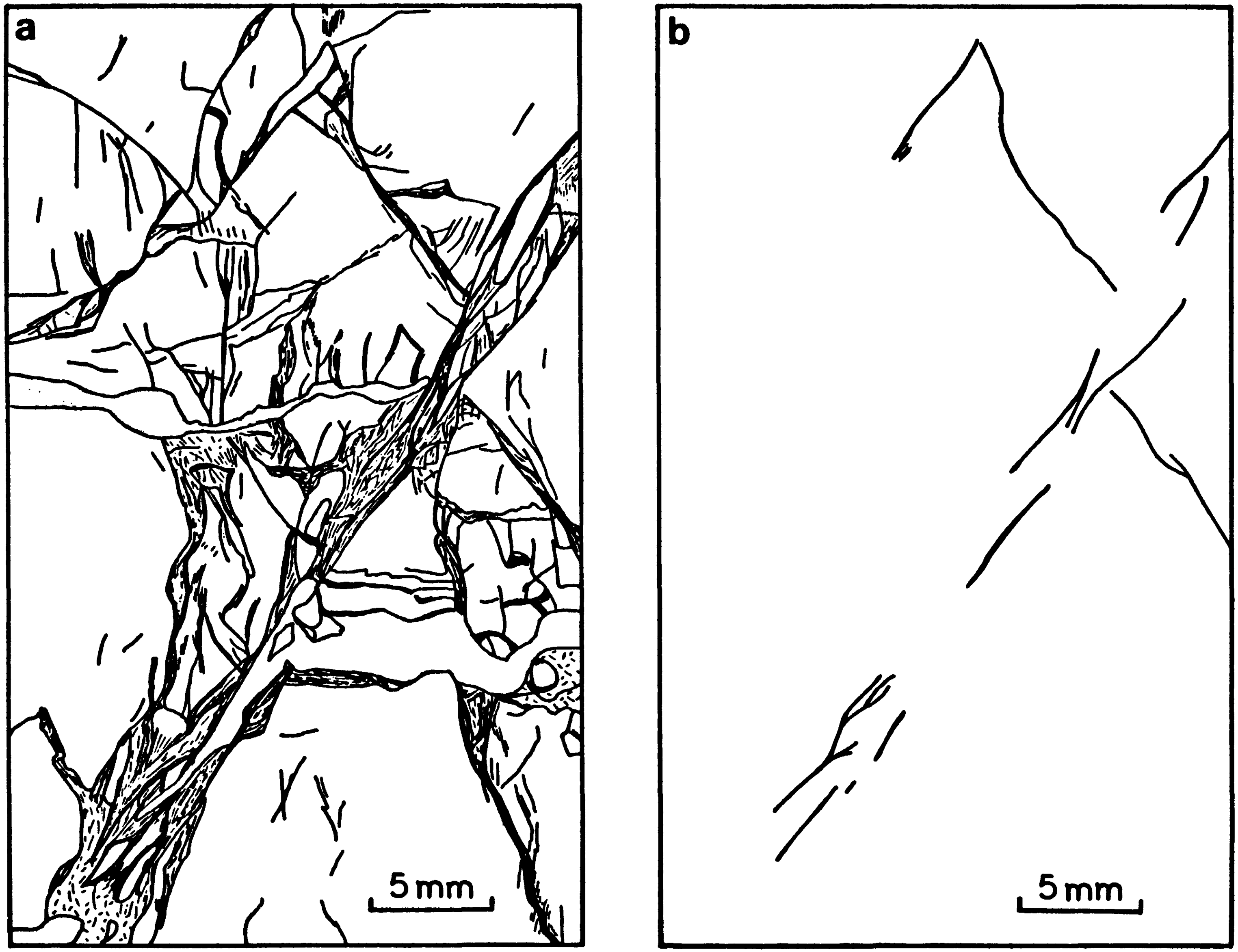

Figure 11. Maps of a) all fractures and b) principal slip paths in Group I sample R90. The complicated fracture pattern surrounding the main fault includes several prominent, conjugate (to nearly perpendicular) and parallel breaks, some of which show evidence of shear as indicated in b).

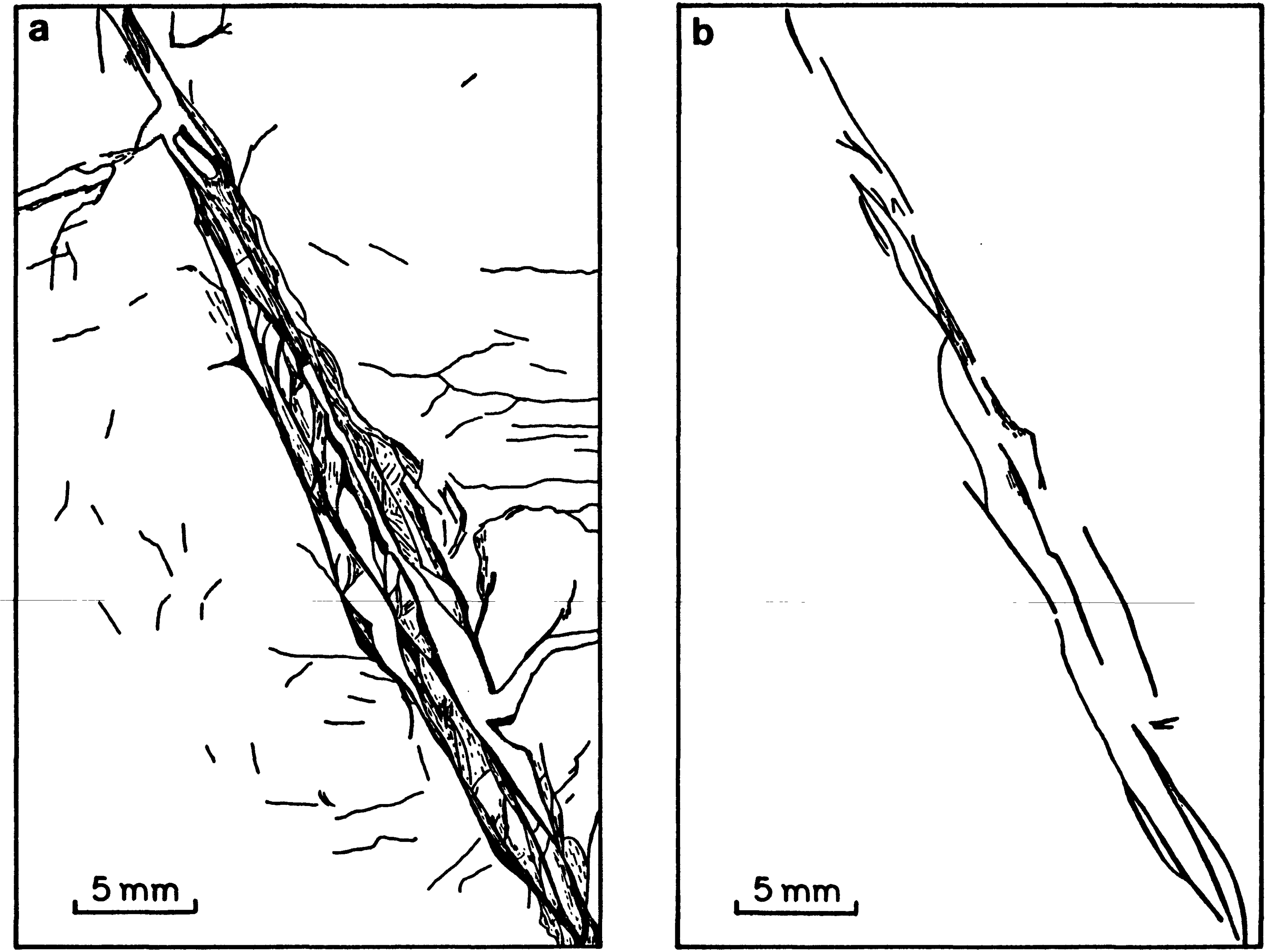

Figure 12. Maps of a) all fractures and b) principal slip paths in Group I sample R91.

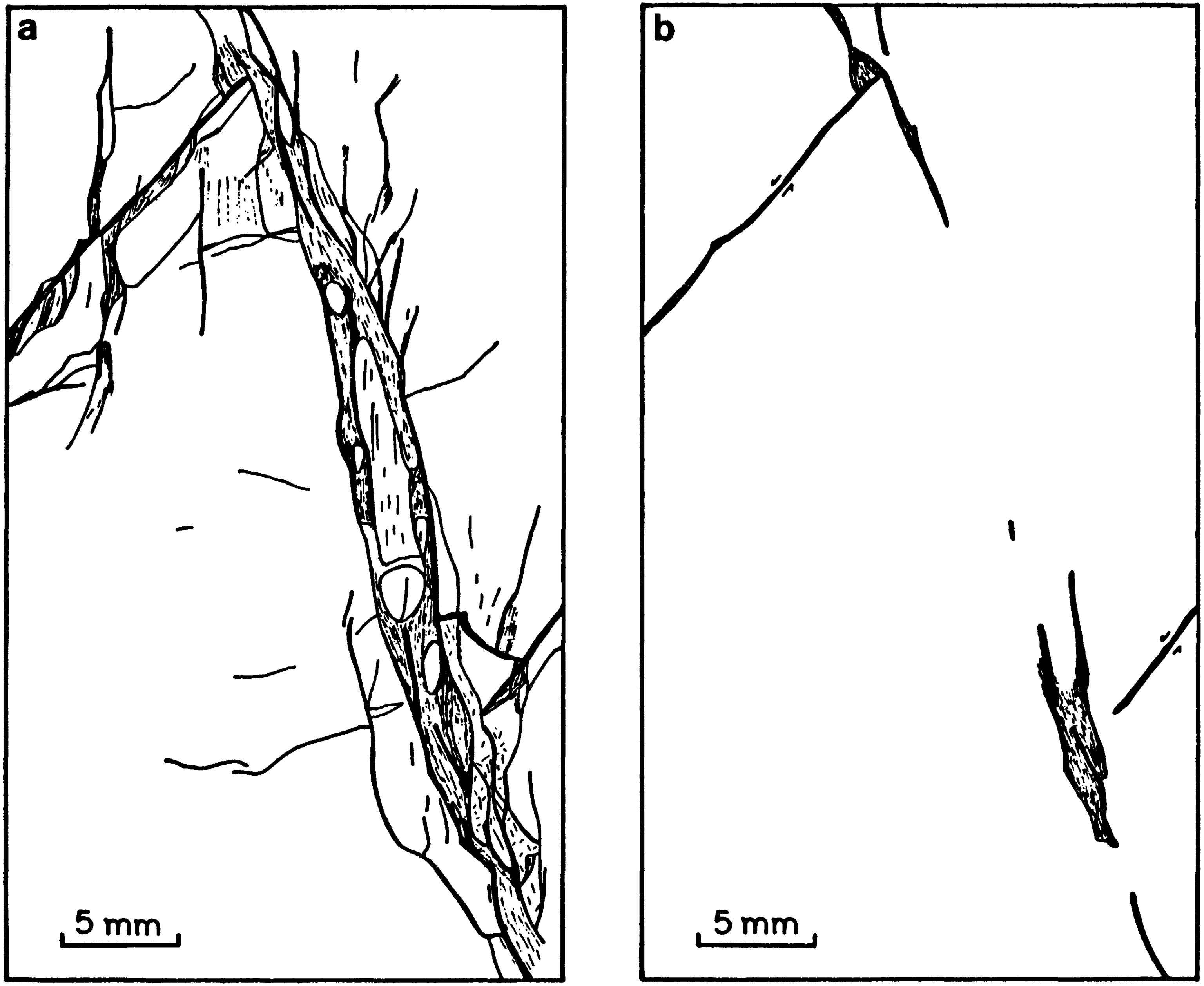

Figure 13. Maps of a) all fractures and b) principal slip paths in Group I sample W2b. The gap in the shear paths in b) coincides with the presence of a brecciated zone; offset may have been distributed across this zone through the movement of grains past each other without, however, producing an increase in the roundness or a decrease in the size of the grains. Such brecciated zones were only observed in the samples run at confining pressures below 100 MPa.

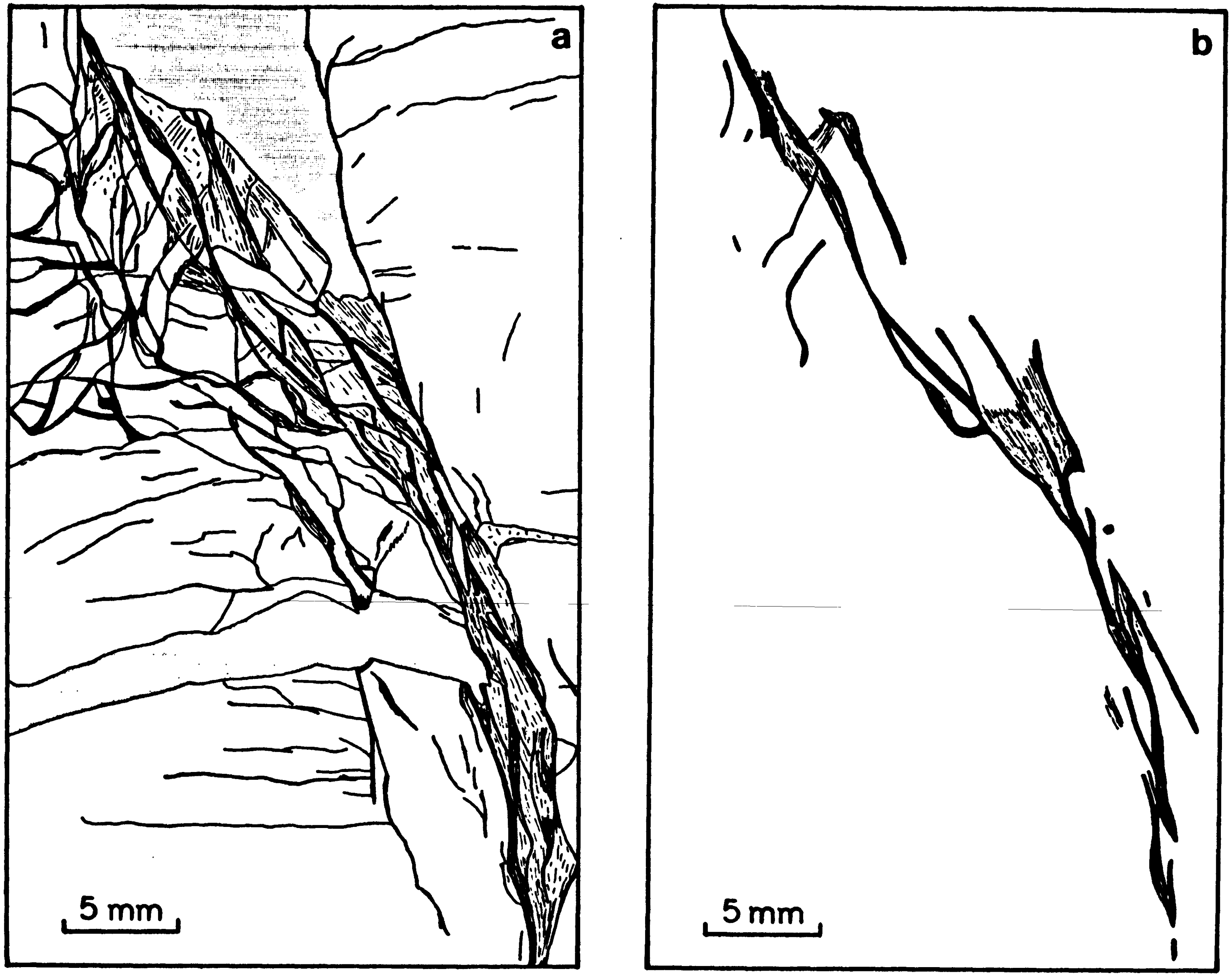

Figure 14. Maps of a) all fractures and b) principal slip paths in Group I sample W3b. Part of the granite adjoining the fault in this sample, and in a few others, as well, has become separated along a horizontal fracture, as shown here by the wide, lightly stippled zone in the lower part of a).

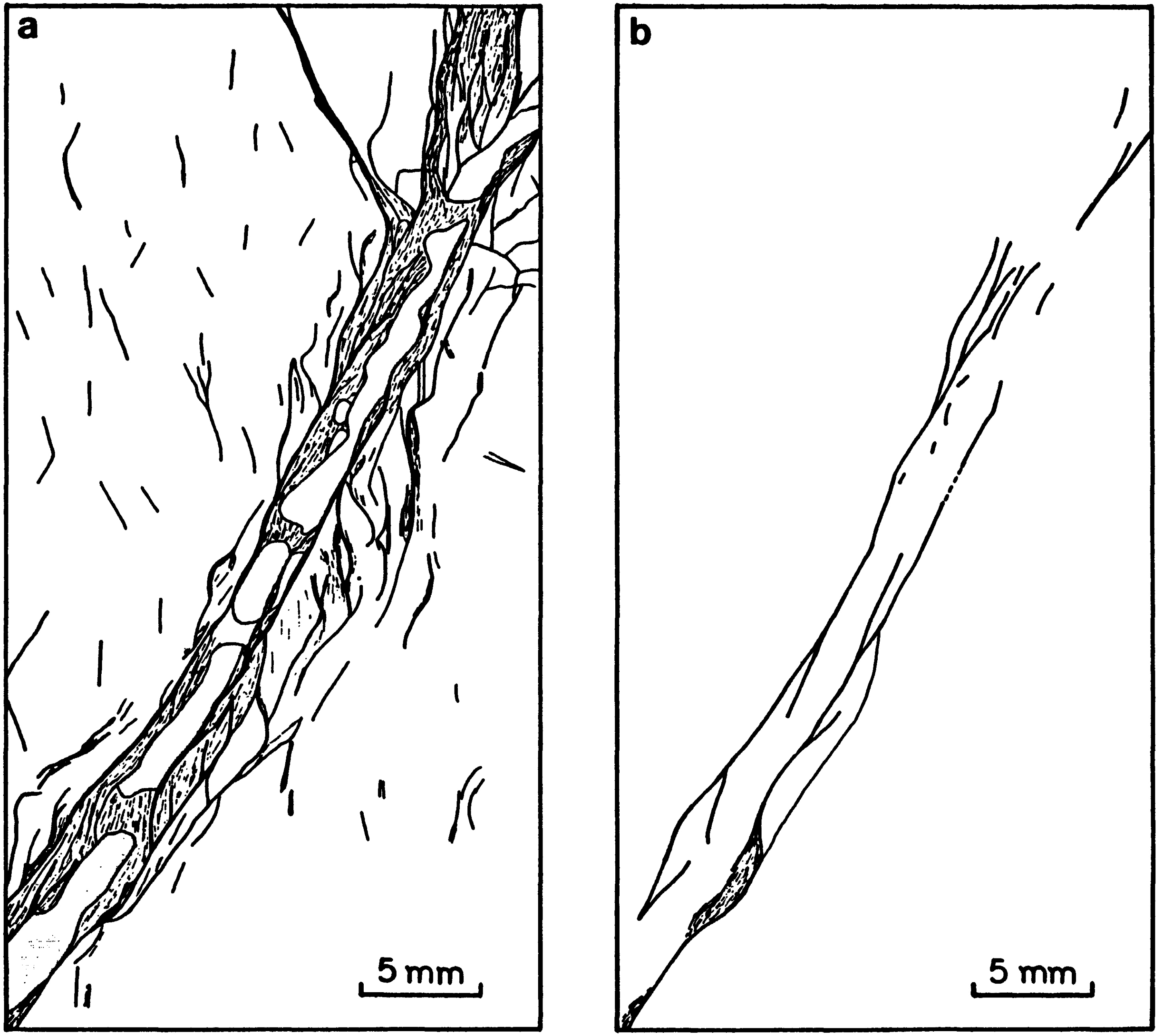

Figure 15. Maps of a) all fractures and b) principal slip paths in Group I sample R120.

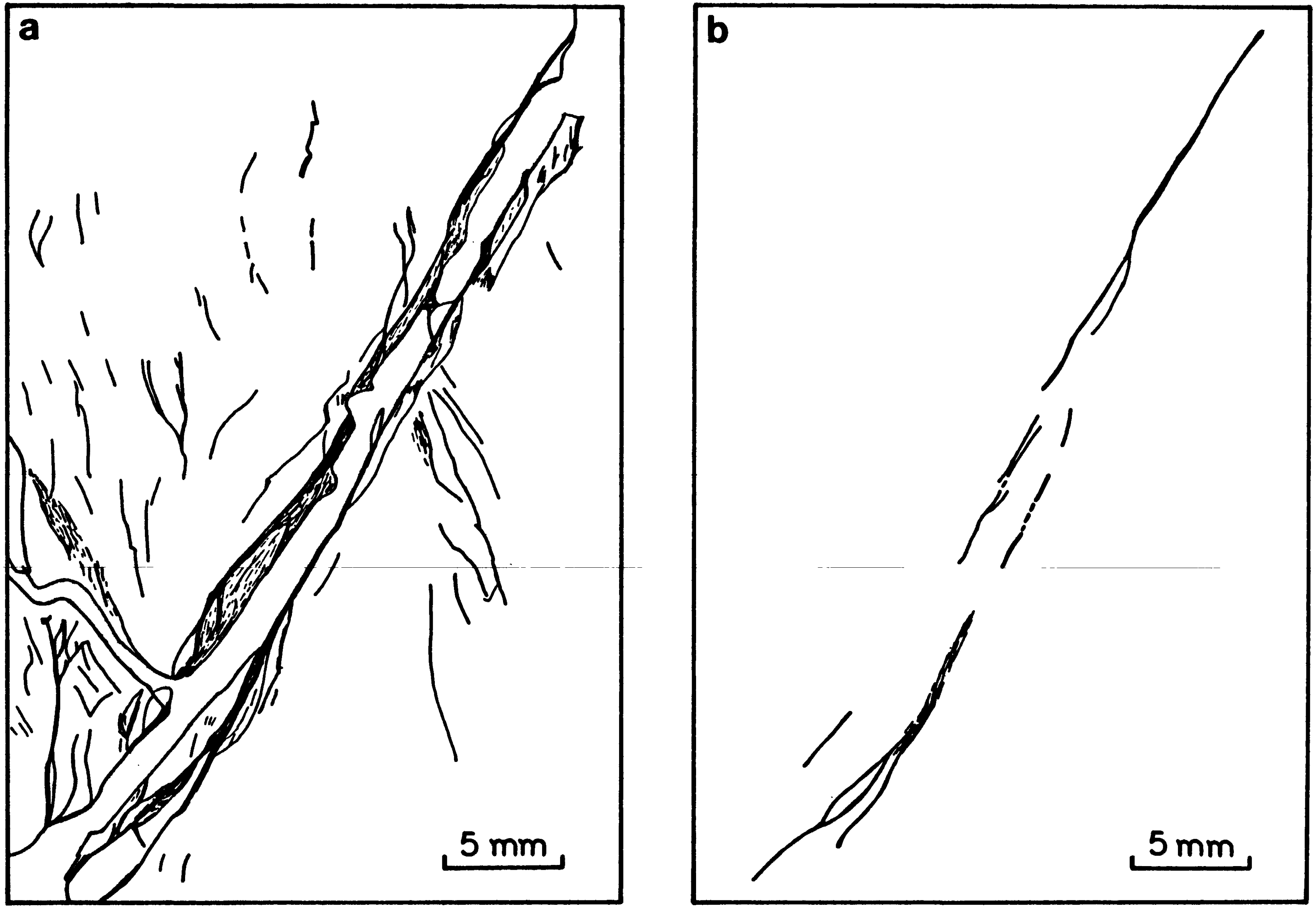

Figure 16. Maps of a) all fractures and b) principal slip paths in Group I sample R122. This experiment terminated unexpectedly at the initial failure of the granite cylinder.

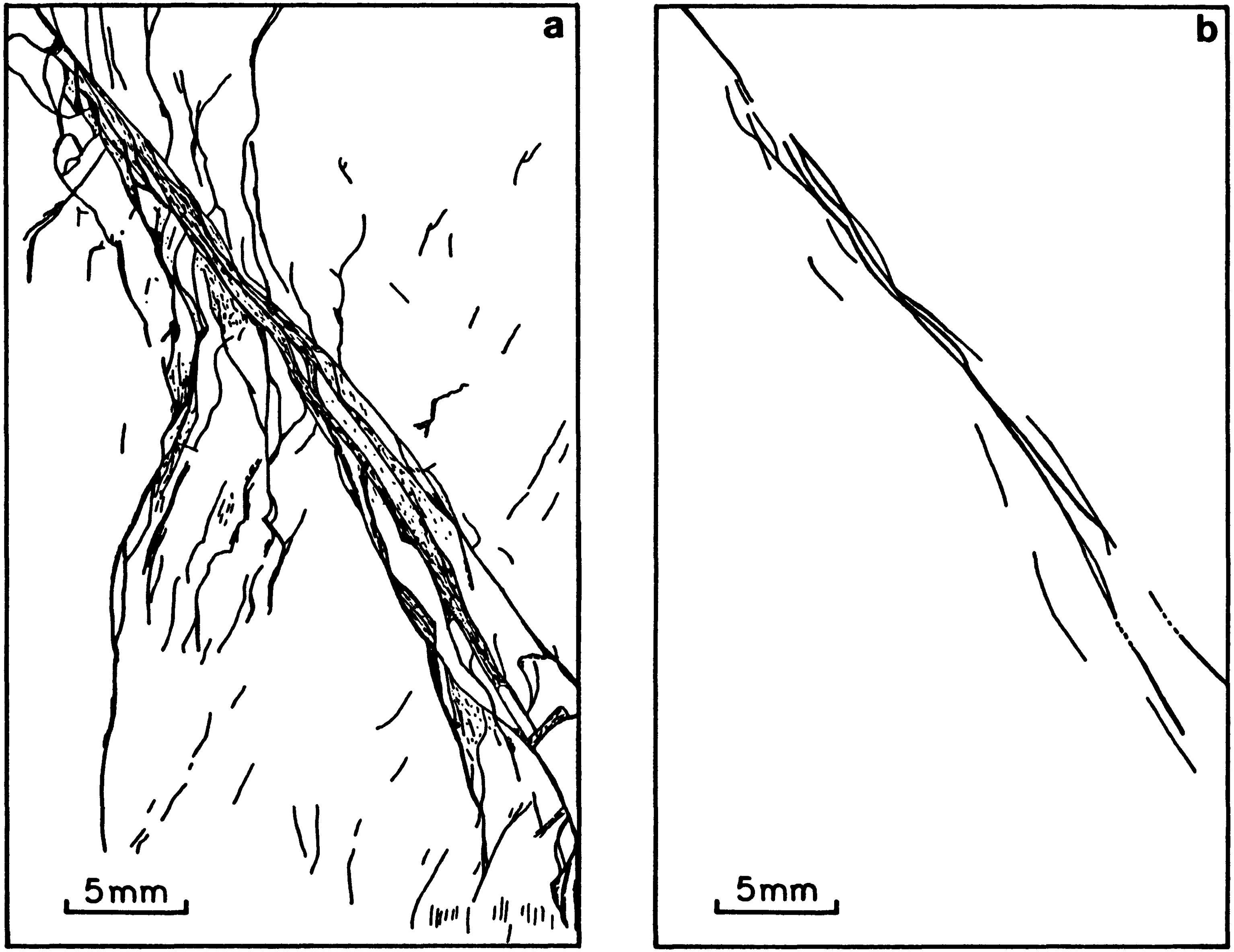

Figure 17. Maps of a) all fractures and b) principal slip paths in Group I sample R123.

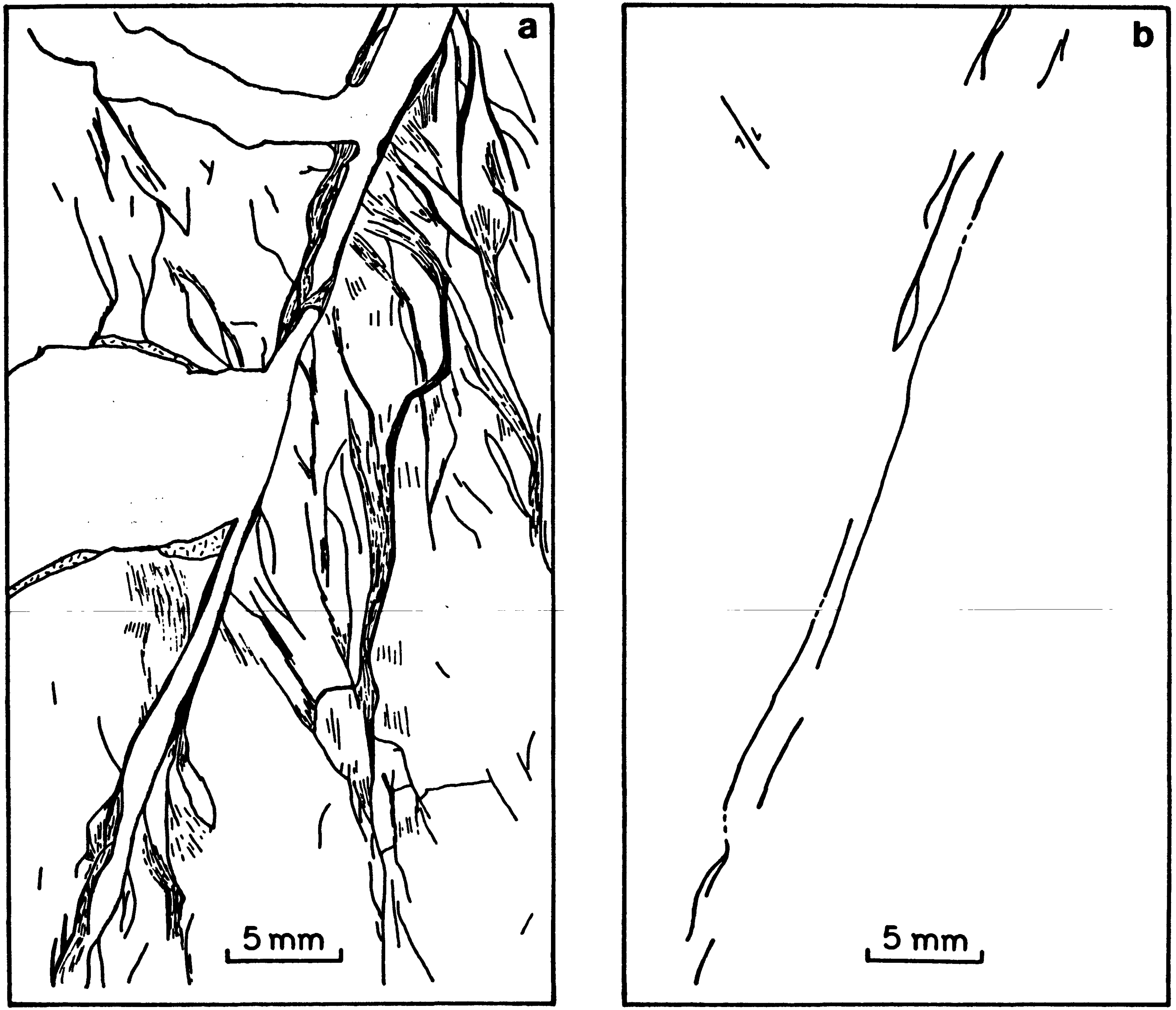

Figure 18. Maps of a) all fractures and b) principal slip paths in Group I sample R125. The granite adjoining the main fault on one side has become separated along two, roughly horizontal fractures.

Figure 19. Map of microfractures in a sample of the Group II Barre starting material. The cut-off length for single fractures in Group II was about 0.5 mm; because of its larger grain size, intragranular fractures are also generally longer in the Group II than in the Group I samples. This section was not prepared at the same time as the other Group II samples; the roughly aligned fractures shown here may therefore have a different orientation from that of the other maps.

Figure 20. Map of microfractures in room-dry, Group II sample RSG1B, which was loaded to 90% of the estimated failure stress at 485 MPa confining pressure.

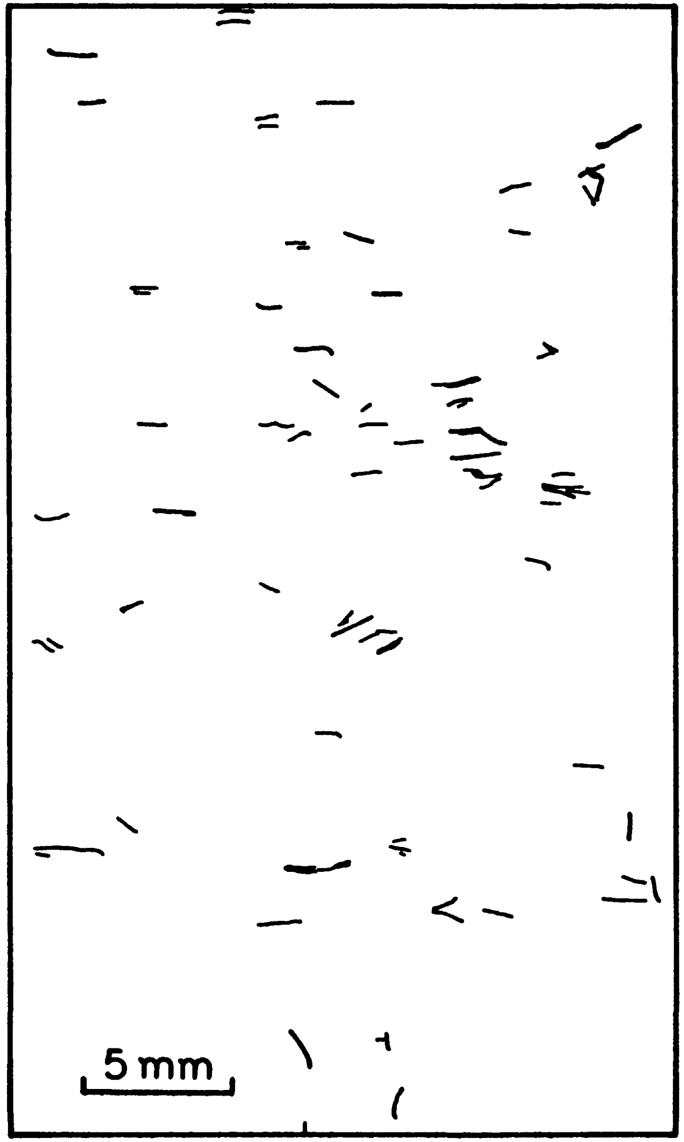

Figure 21. Map of microfractures in room-dry, Group II sample RSG2B, which was loaded to 67% of the failure stress for a confining pressure of 485 MPa.

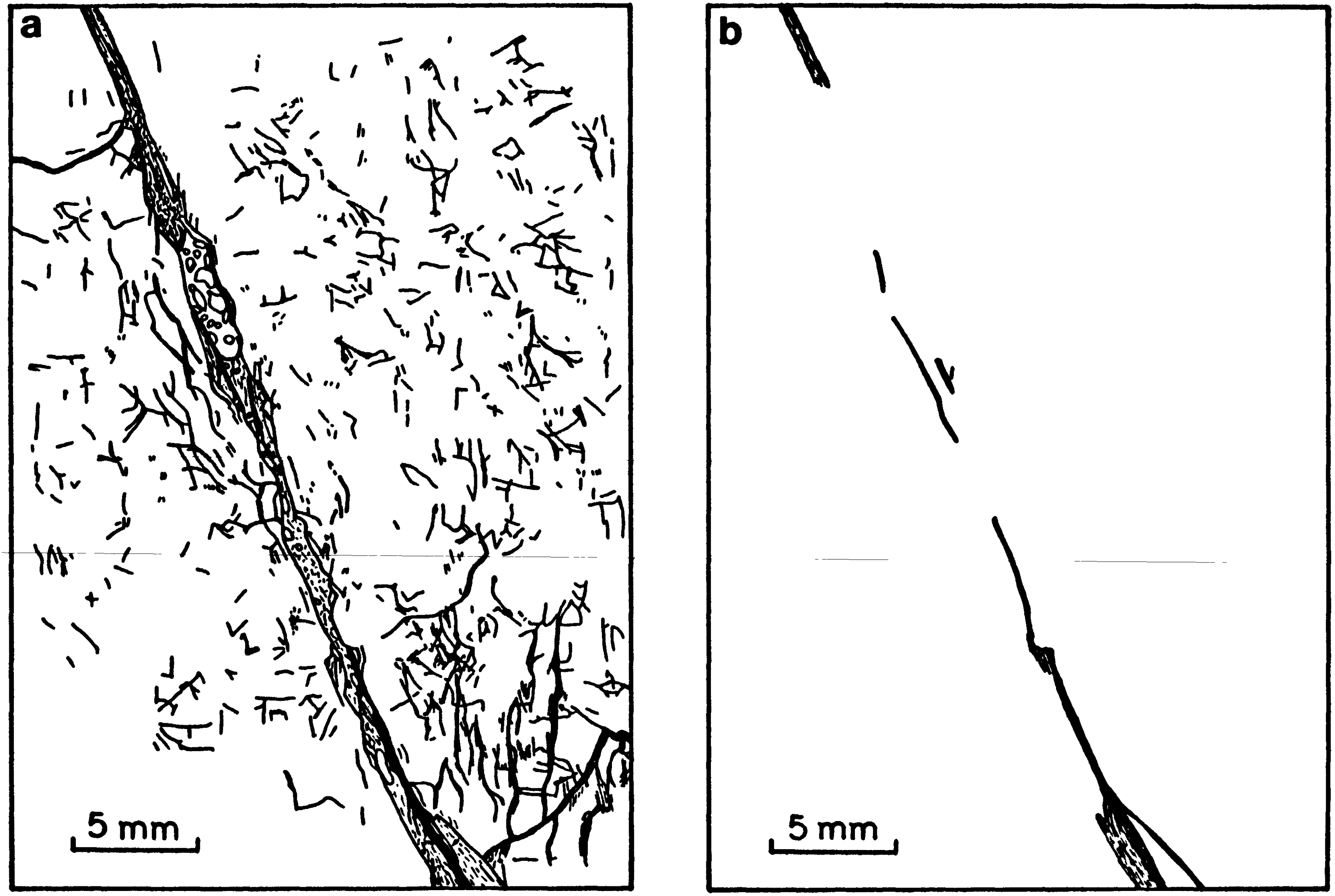

Figure 22. Maps of a) all fractures and b) principal slip paths in Group II sample RSG3B. This sample contains brecciated zones similar to that described for Group I sample W2b (Fig. 13).

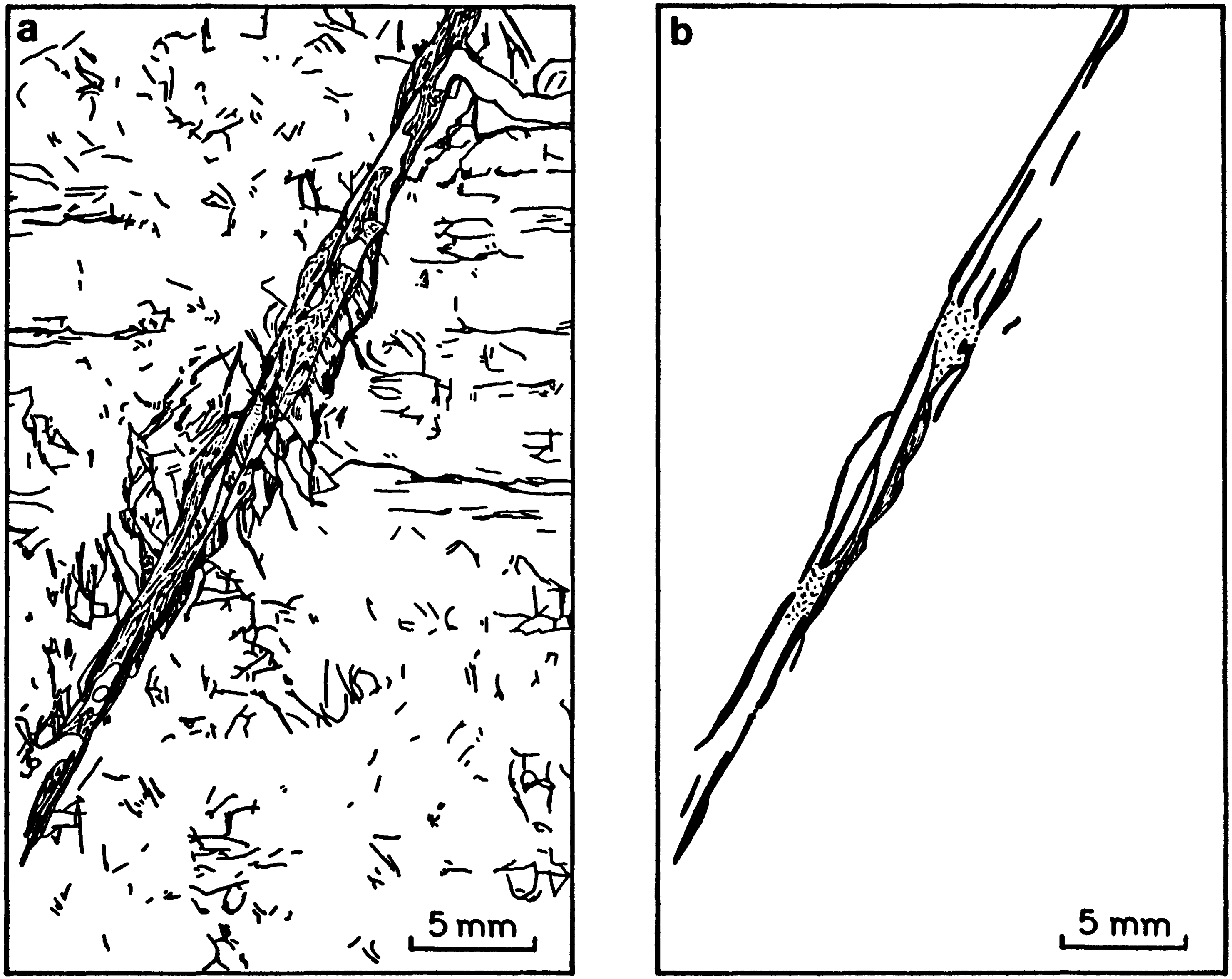

Figure 23. Maps of a) all fractures and b) principal slip paths in Group II sample RSG4B. The granite surrounding the main faults in the Group II samples contains many clusters of short fractures that commonly bend around to form a partially to completely closed space. These clusters are groups of intragranular and grain-boundary fractures that are principally developed in quartz.

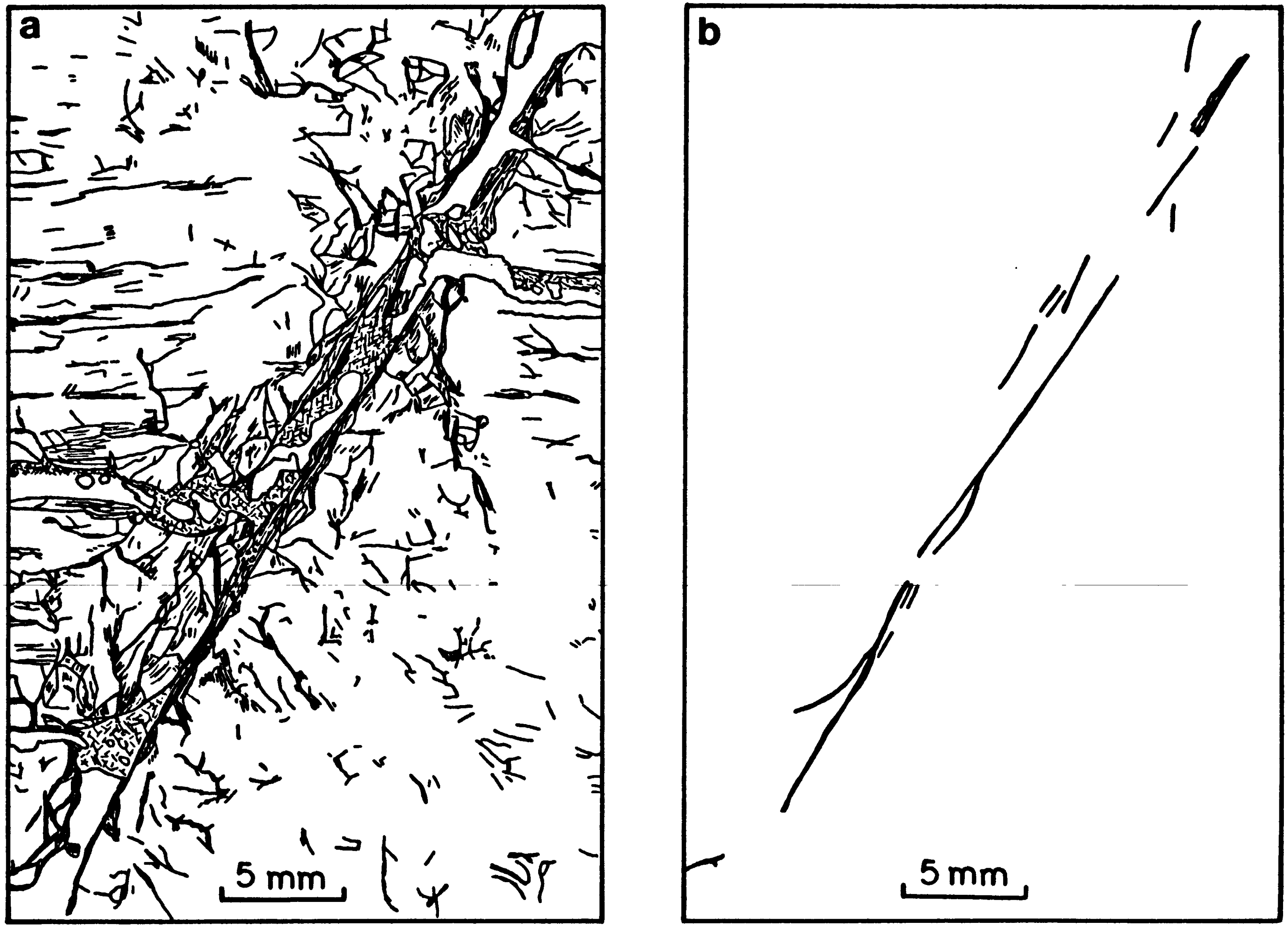

Figure 24. Maps of a) all fractures and b) principal slip paths in Group II sample RSG5B.

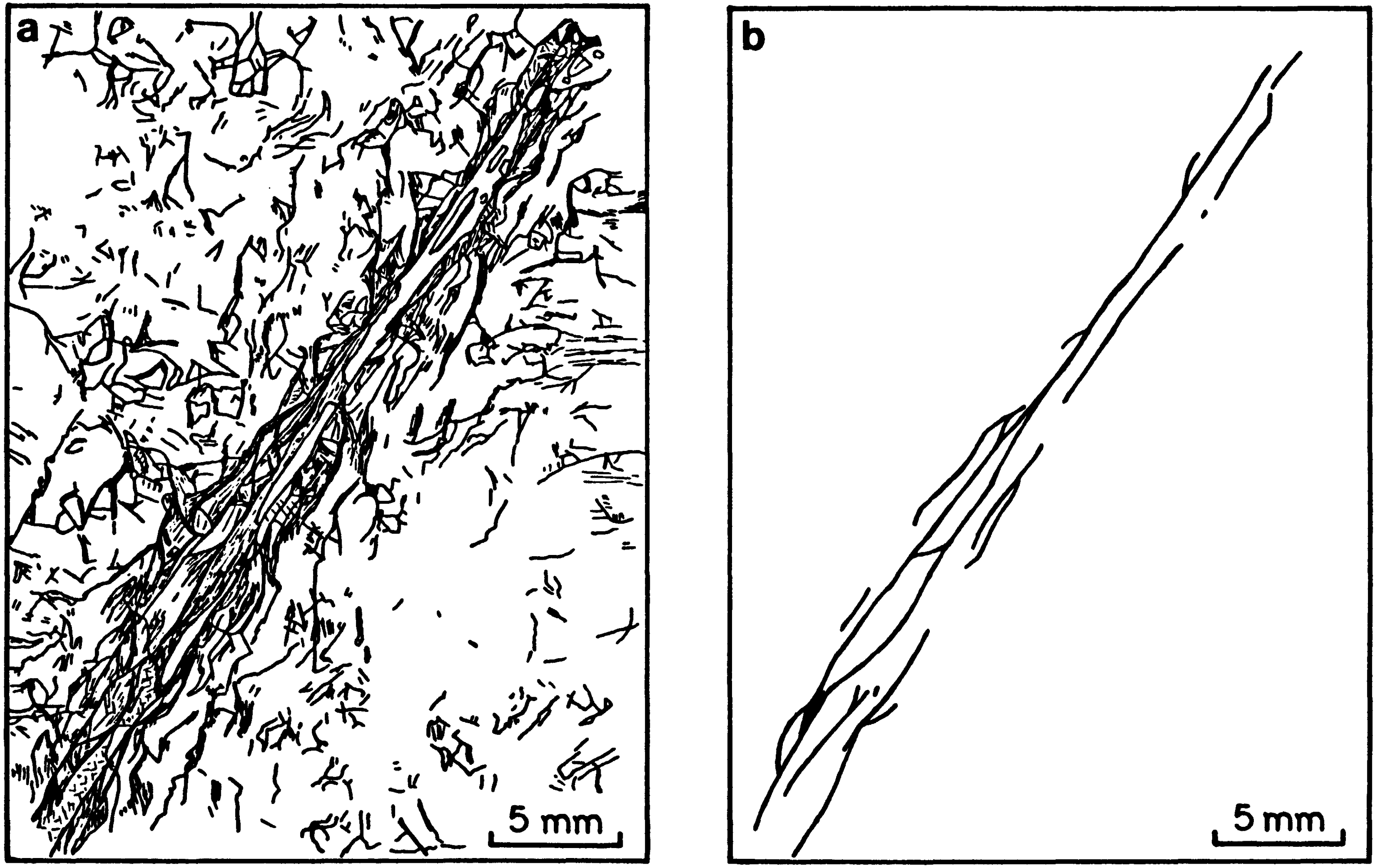

Figure 25. Maps of a) all fractures and b) principal slip paths in Group II sample RSG6B.

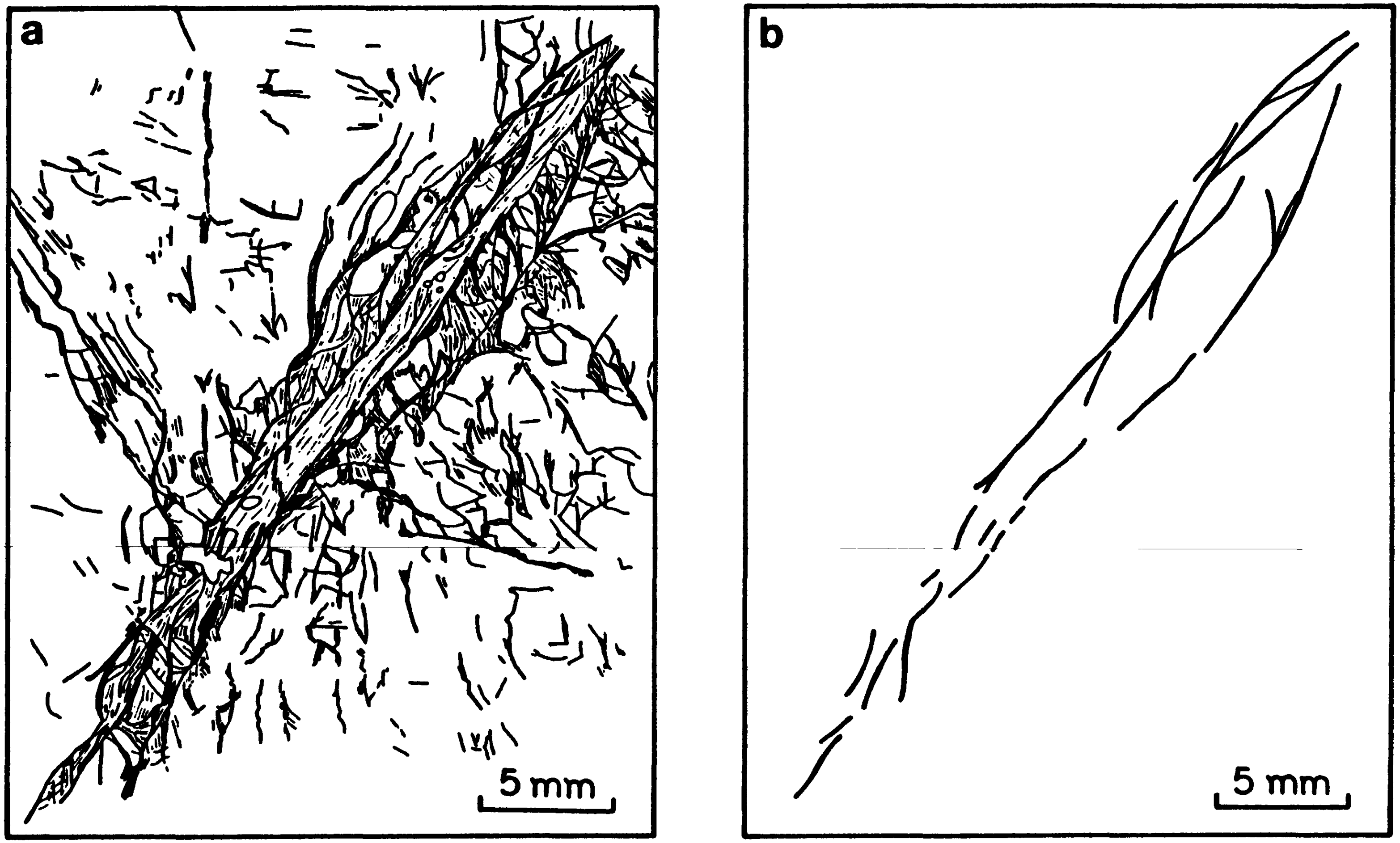

Figure 26. Maps of a) all fractures and b) principal slip paths in Group II sample RSG7B.

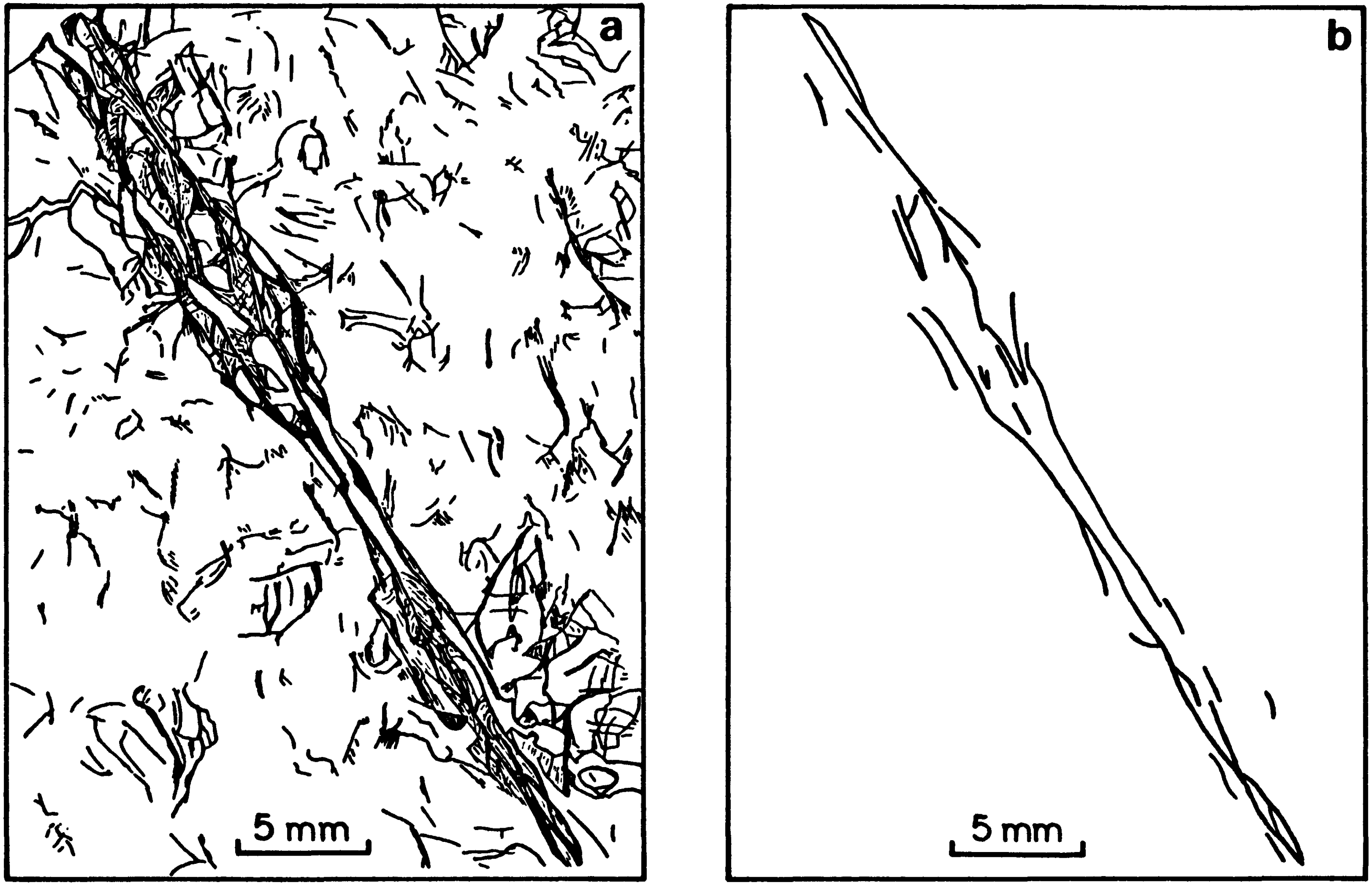

Figure 27. Maps of a) all fractures and b) principal slip paths in Group II sample RSG8B.

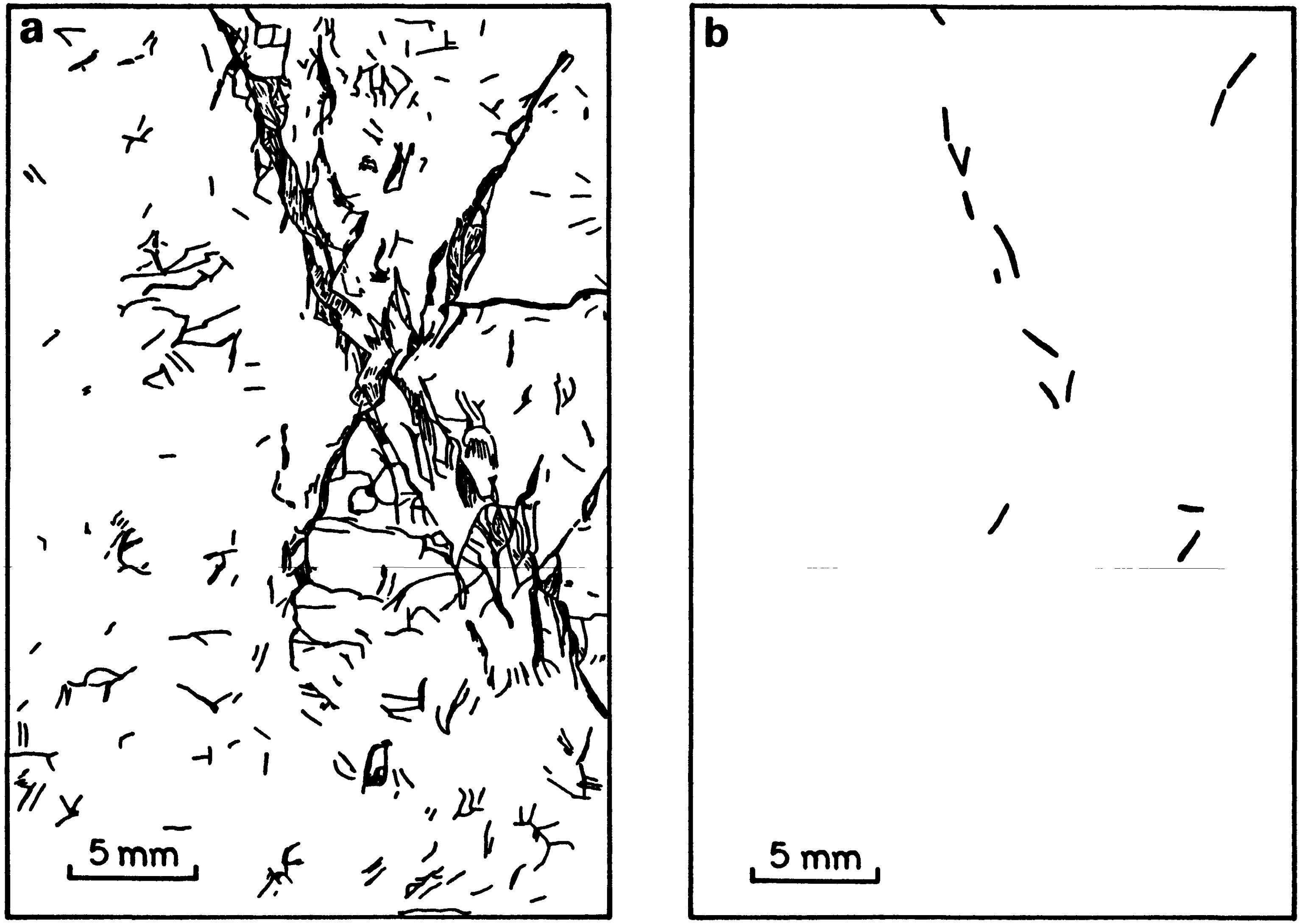

Figure 28. Maps of a) all fractures and b) principal slip paths in Group II sample RSG9B, which was loaded to the failure point at 100 MPa confining pressure. A conjugate break is nearly as well developed as the main fault in this sample. The map of slip paths in b) consists of a set of short, unconnected lines.

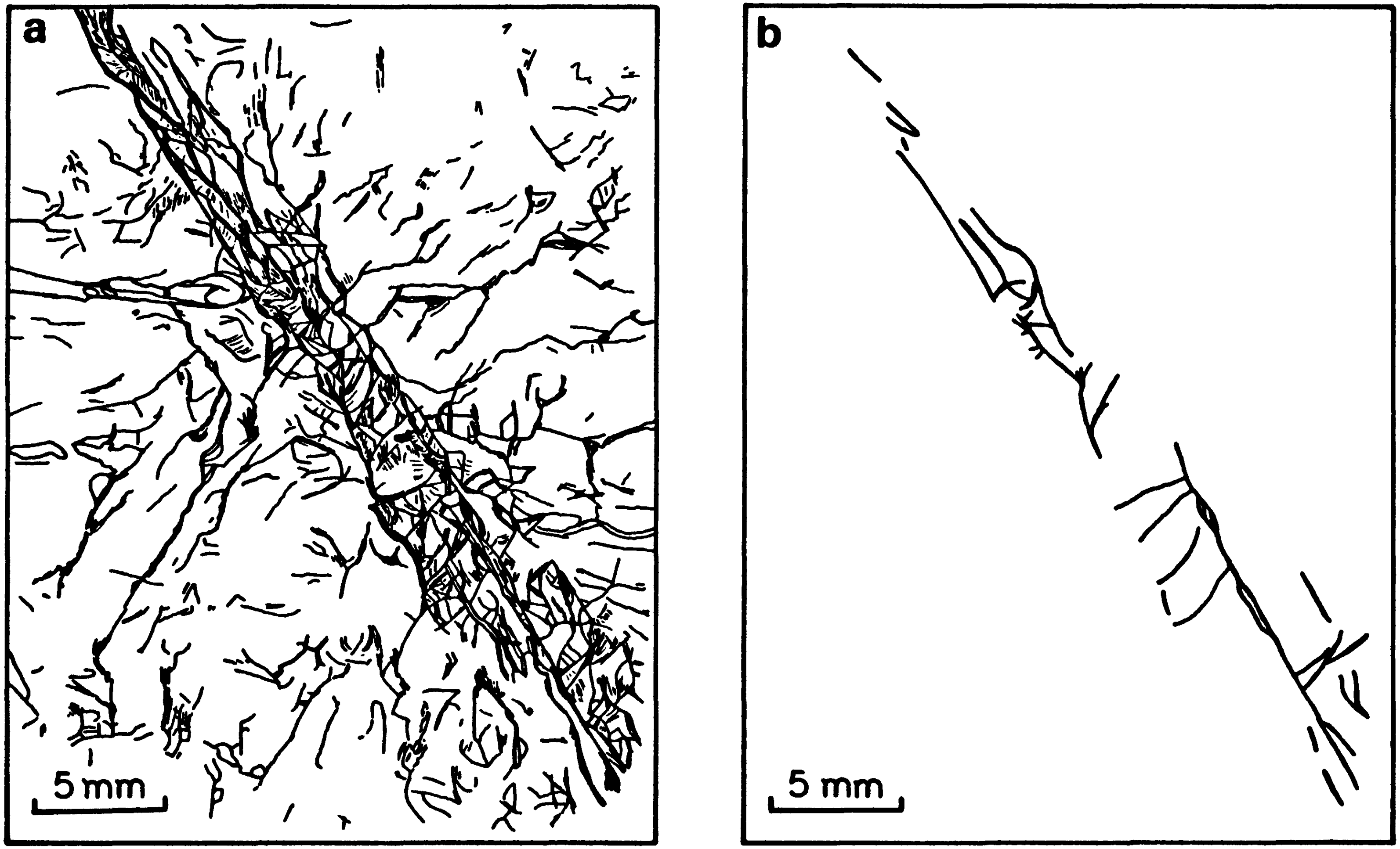

Figure 29. Maps of a) all fractures and b) principal slip paths in Group II sample RSG10B, which was loaded to the failure point at 500 MPa confining pressure. The fracturing accompanying this break is more complicated than that shown in the lower-pressure sample of Figure 28a.

Figure 30. Map of microfractures in pre-saturated, Group II sample RSG11B, which was loaded to 90% of the estimated failure stress at 500 MPa confining pressure.

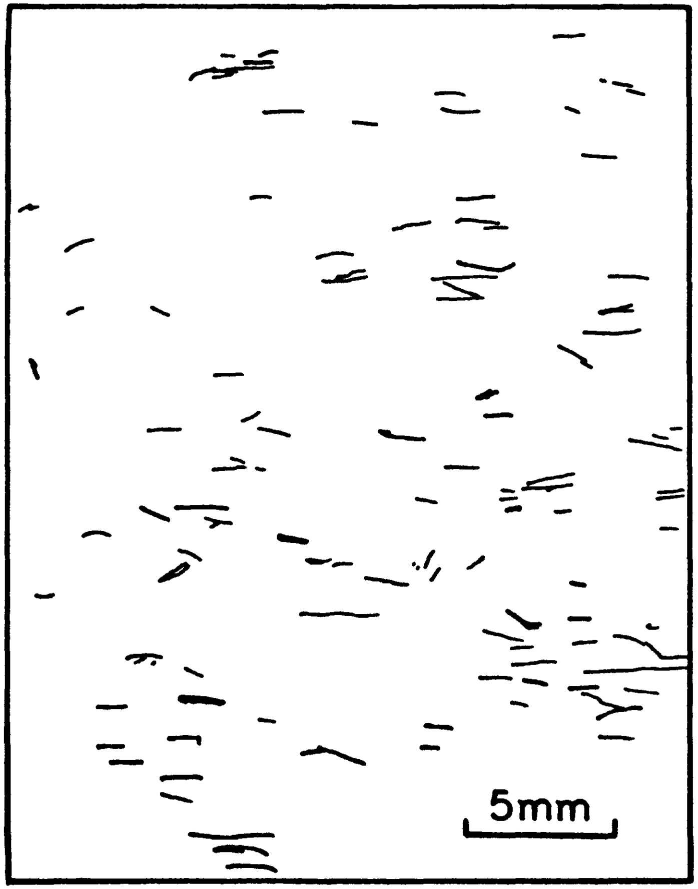

Figure 31. Map of microfractures in pre-saturated, Group II sample RSG12B, which was loaded to 67% of the failure stress for a confining pressure of 500 MPa.

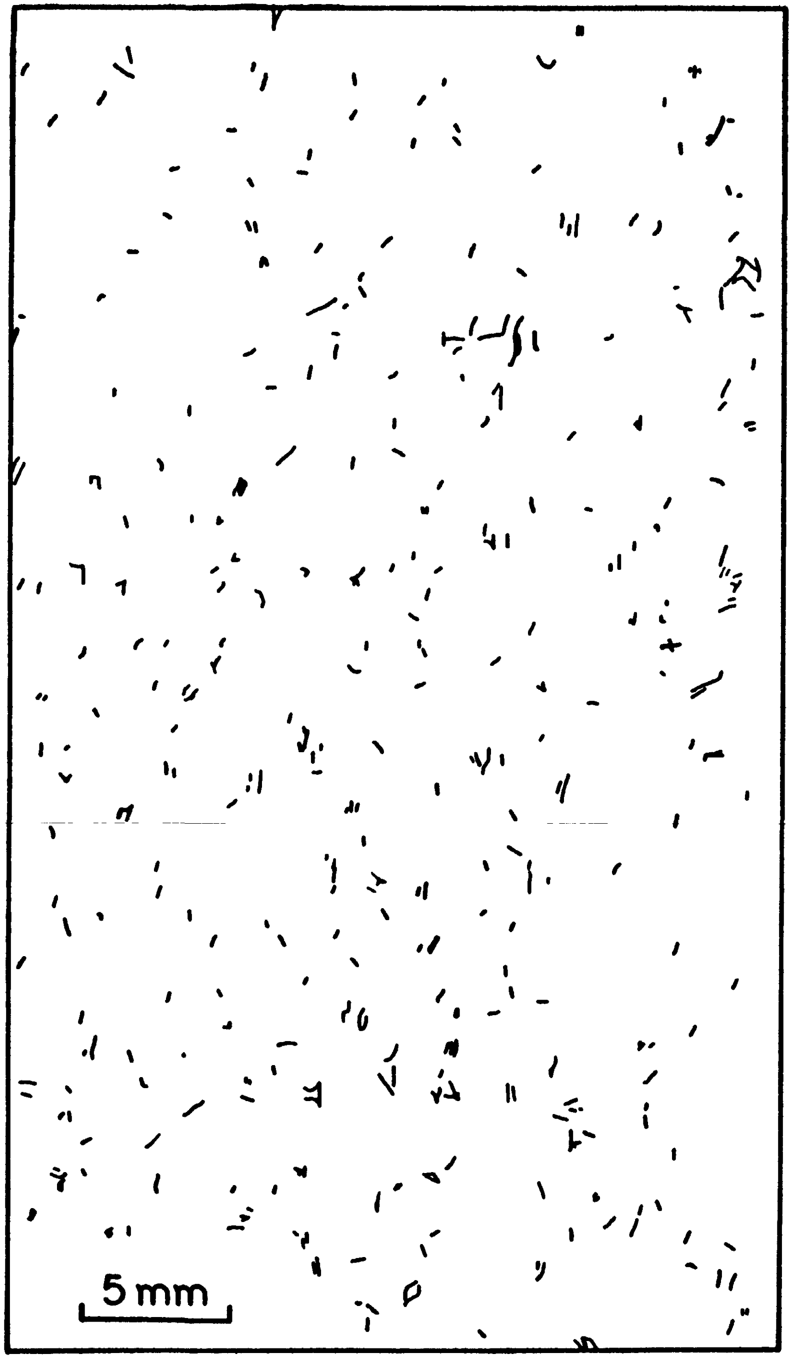

Figure 32. Maps of microfractures in a sample of the Group III Westerly starting material. The cut-off length for mapping single fractures in Group III was about 0.25 mm, leading to a greater density of fracturing than in Figure 6.

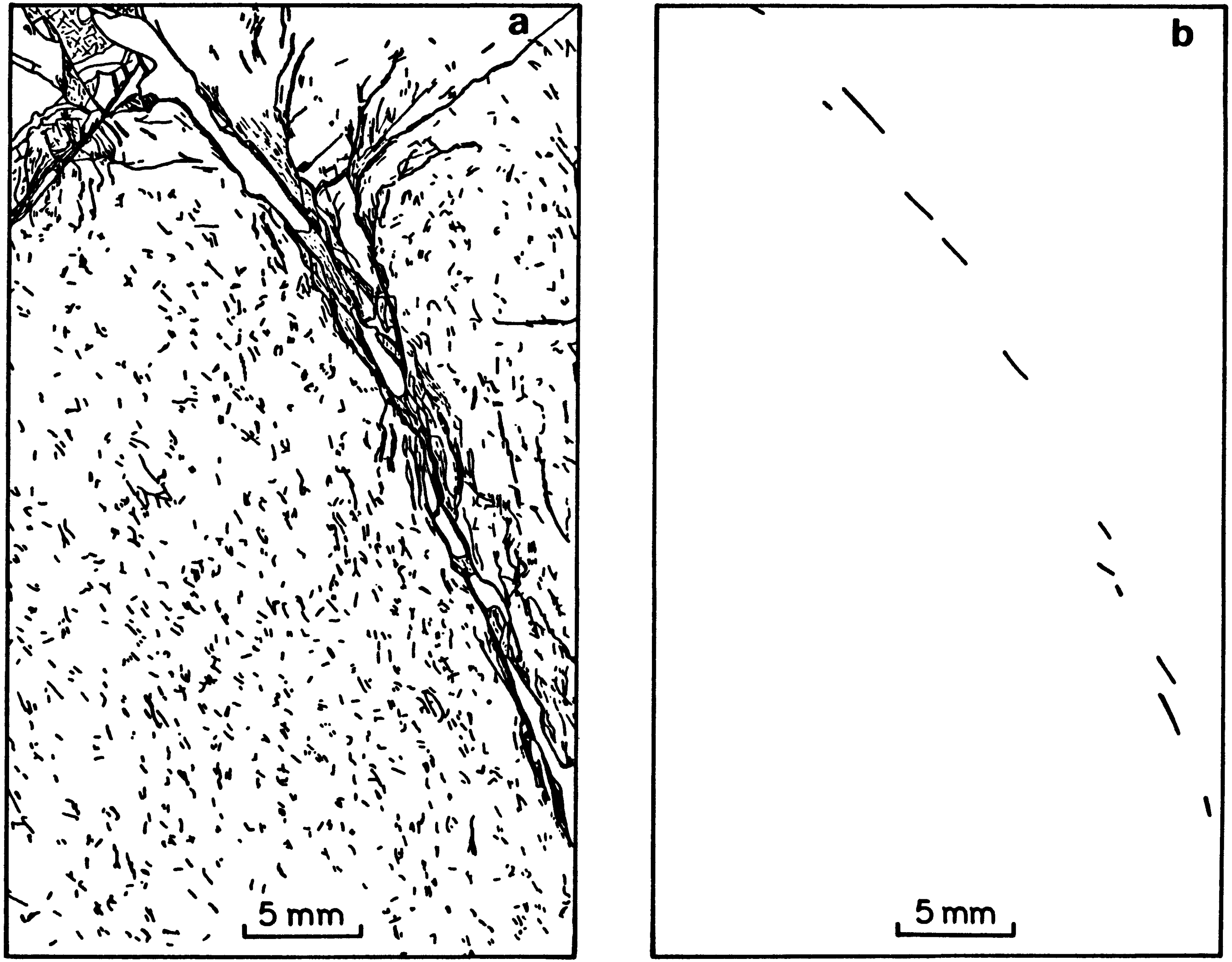

Figure 33. Maps of a) all fractures and b) principal slip paths in Group III sample RSG501, which was loaded to the failure point at 100 MPa confining pressure. The map of slip paths in b) is a set of short, unconnected lines.

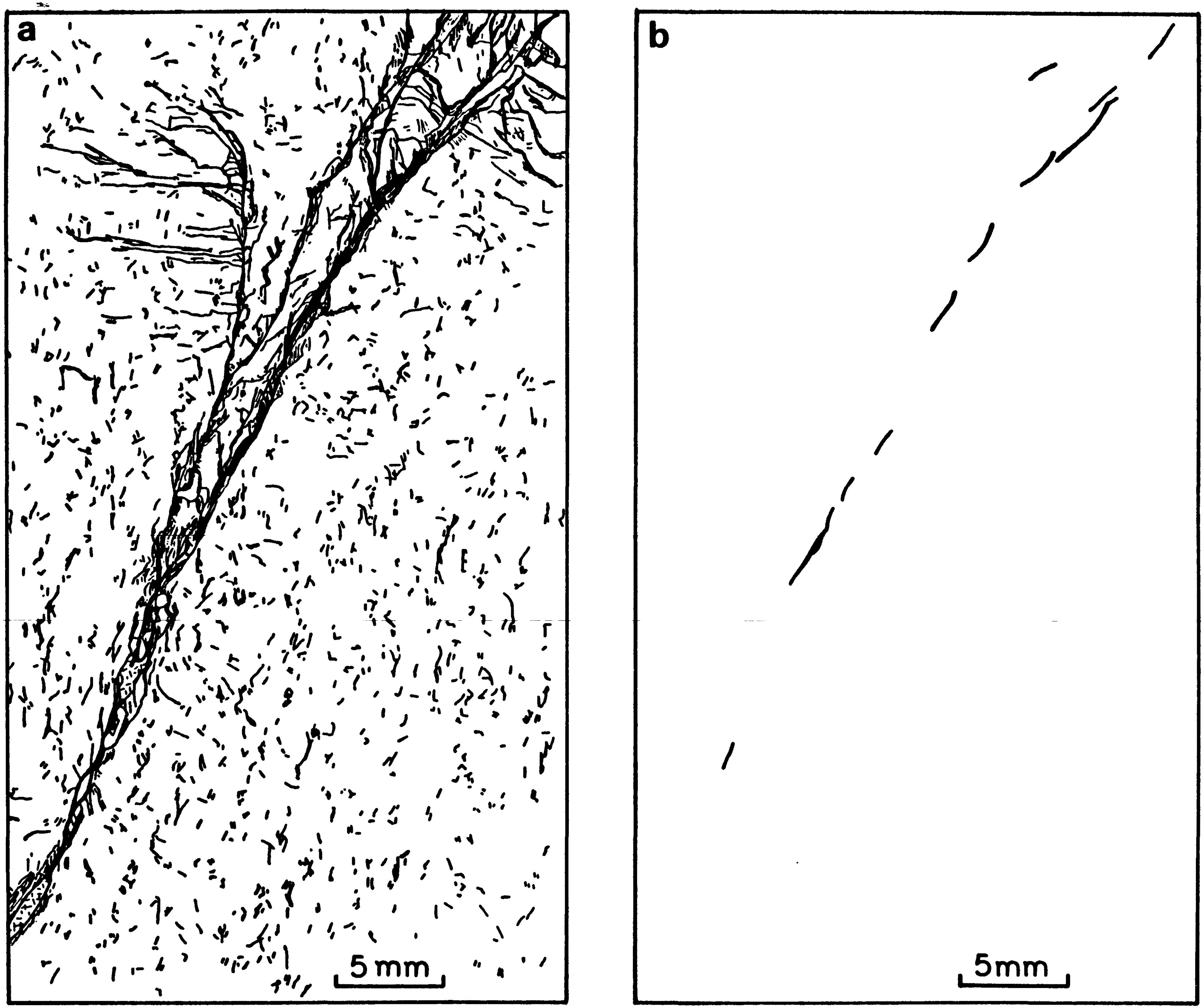

Figure 34. Maps of a) all fractures and b) principal slip paths in Group III sample RSG502, which was loaded to the failure point at 100 MPa confining pressure.

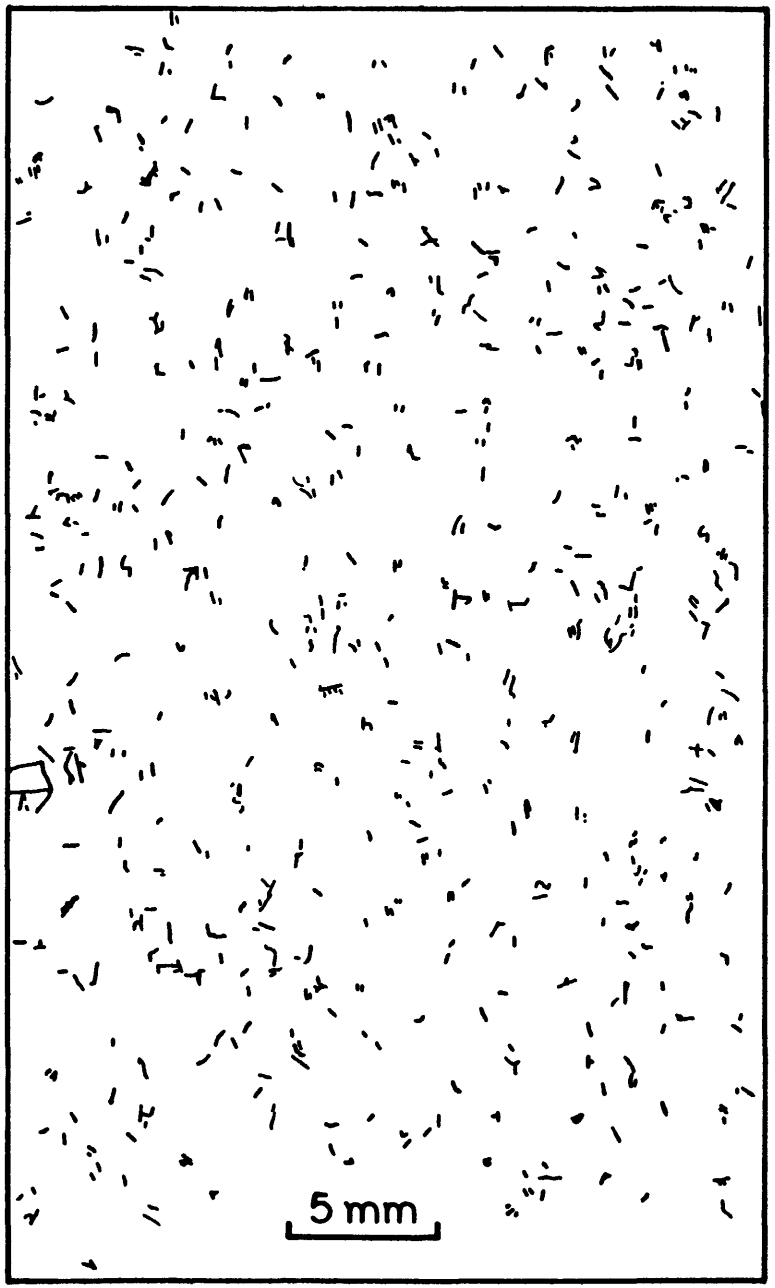

Figure 35. Map of microfractures in Group III sample RSG503, which was loaded to 99% of the estimated failure stress at 100 MPa confining pressure.

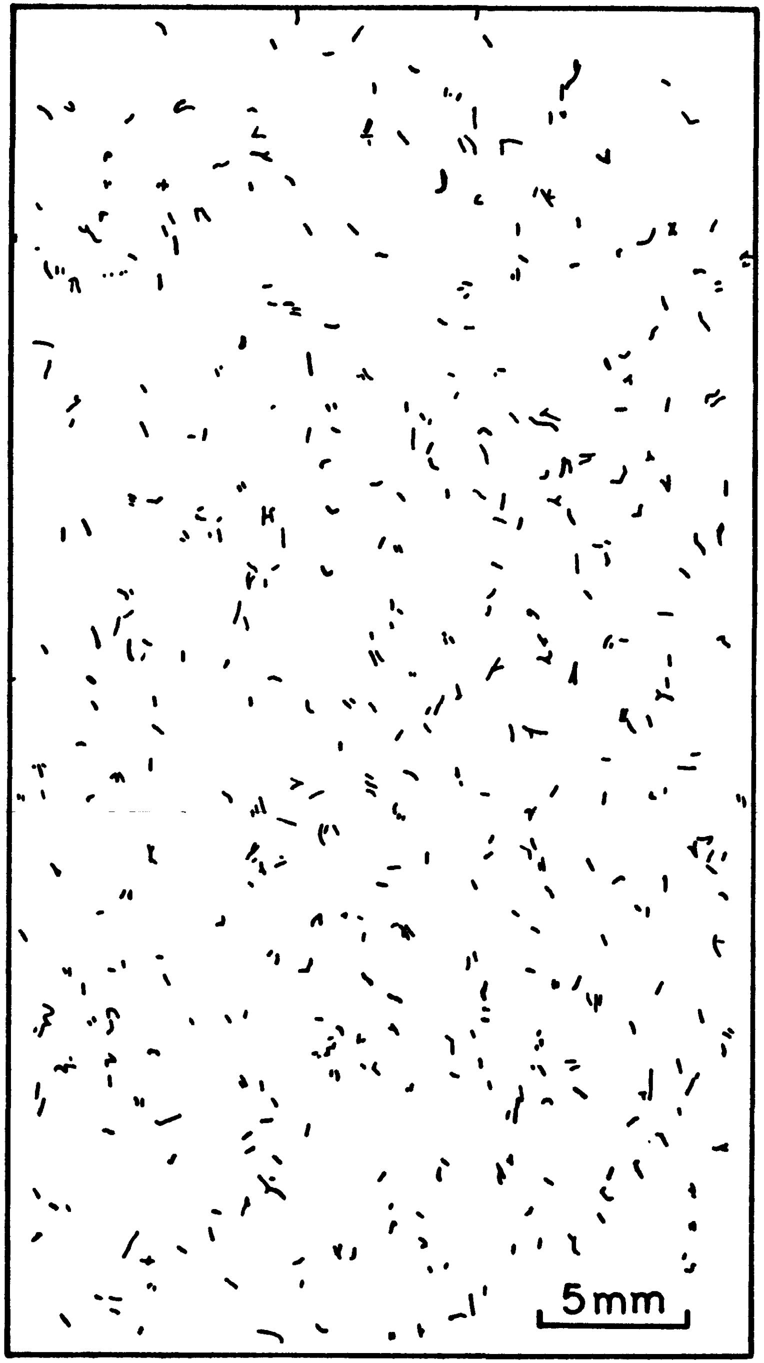

Figure 36. Map of microfractures in Group III sample RSG504, which was loaded to 90% of the failure stress for a confining pressure of 100 MPa.

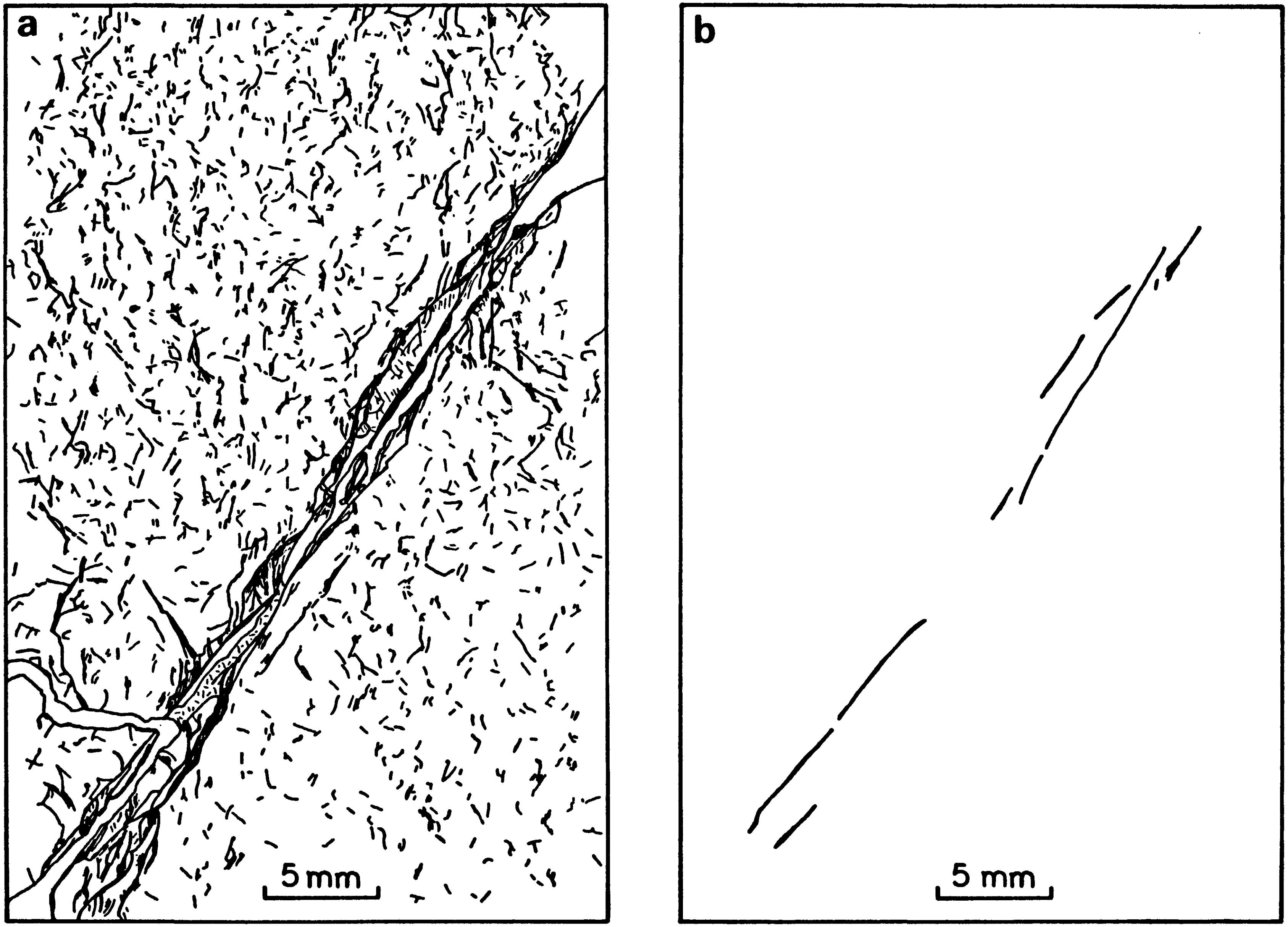

Figure 37. Maps of a) all fractures and b) principal slip paths in Group III sample RSG505, which was loaded to the failure point at 500 MPa confining pressure. Note the increased density of microfracturing in a), compared to the maps of lower-pressure samples in Figures 33a and 34a.

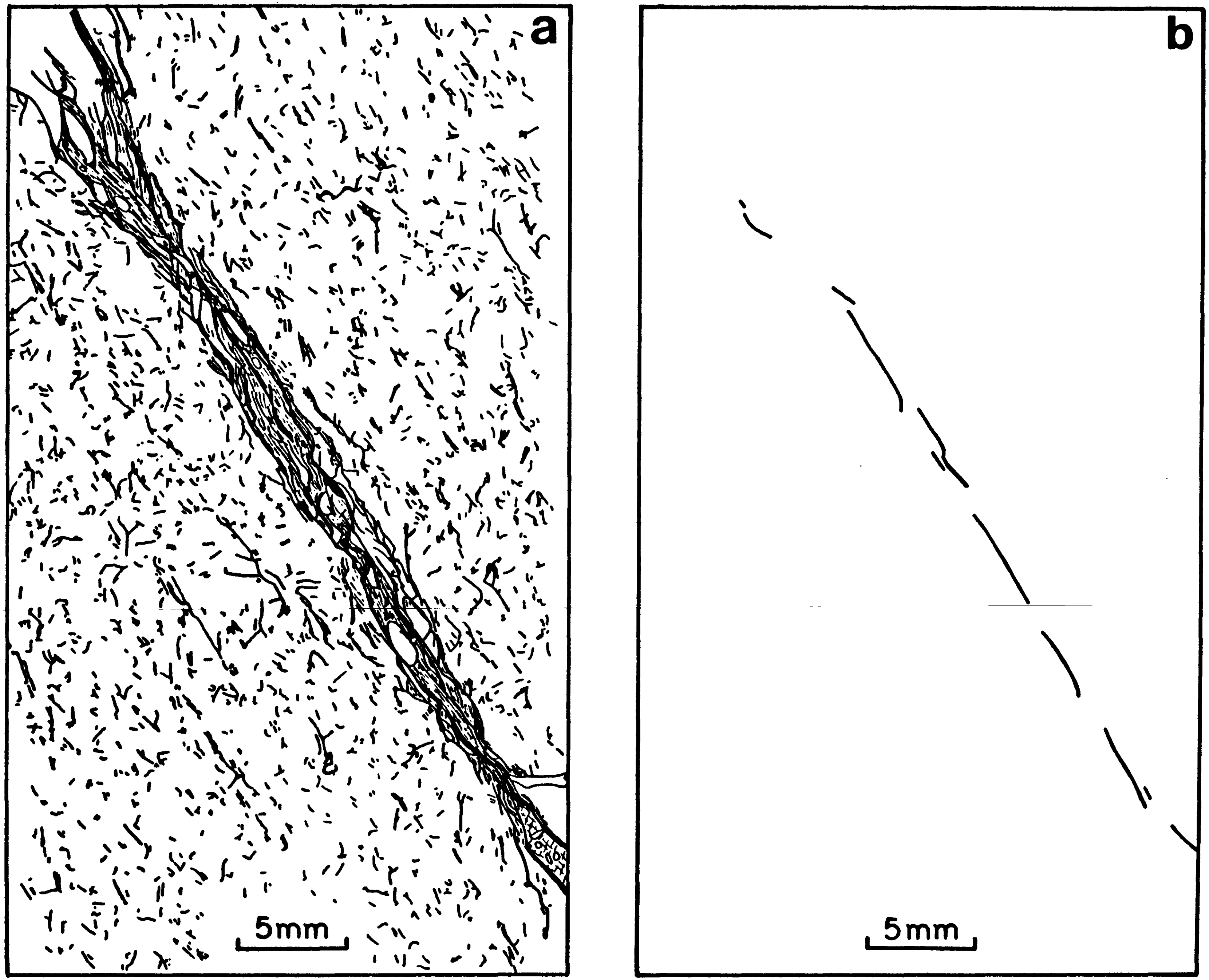

Figure 38. Maps of a) all fractures and b) principal slip paths in Group III sample RSG506, which was loaded to the failure point at 500 MPa confining pressure.

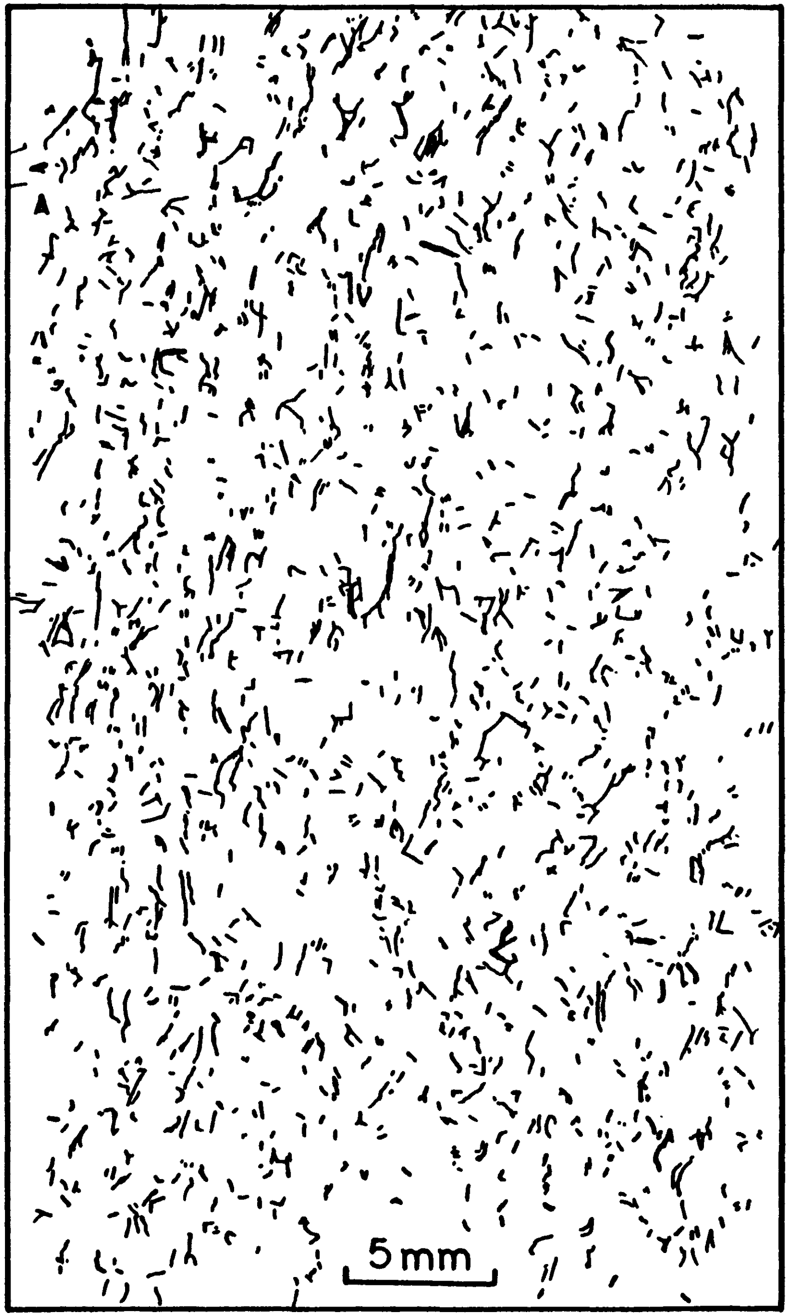

Figure 39. Map of microfractures in Group III sample RSG507, which was loaded to 99% of the estimated failure stress at 500 MPa confining pressure.

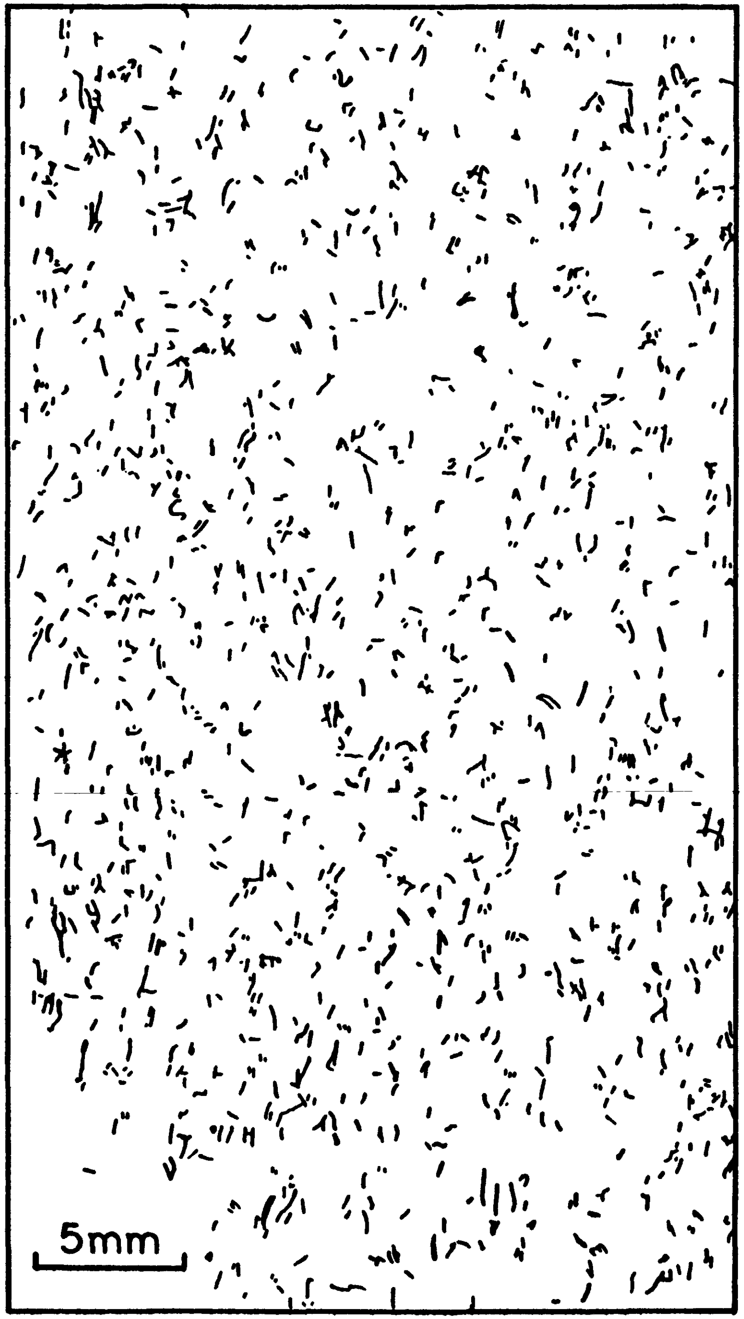

Figure 40. Map of microfractures in Group III sample RSG508, which was loaded to 90% of the failure stress for a confining pressure of 500 MPa.

sectioning process are indicated on the maps of all fractures by a light, stippled pattern.

The density of fracturing around the principal fault zone varies from sample to sample, without any observable trends. Most of the surrounding fractures can be classified into one of 5 orientations: parallel, conjugate, or perpendicular to the orientation of the principal fault, or parallel or perpendicular to the axis of the granite cylinder (termed 'vertical' and 'horizontal', respectively, corresponding to their orientation in the deformation maps). These 5 fracture types are illustrated in Figure 41. For those samples whose main fault zones formed at a relatively large angle to the cylinder axis (roughly 35° or more; see next section for fault zone orientations), the perpendicular and conjugate fractures will have similar orientations and as a result will be indistinguishable.

Qualitative examination of the deformation maps suggests that the relative abundances of the 5 fracture types in a given sample may be a function of the confining pressure. The horizontal fractures were most frequently observed in samples run at confining pressures of 313 MPa or less (e.g., Figs. 7, 14). The conjugate fractures were common in all but the lowest-pressure (40 and 50 MPa) samples, and parallel fractures were scattered among all the samples. The vertical and perpendicular fractures were almost mutually exclusive in their occurrence: the vertical fractures were abundant at low (less than 100 MPa) and high (300 MPa or more) pressures (e.g., Figs., 22, 26), whereas the perpendicular fractures were most abundant in the intermediate range (roughly 100 to 313 MPa) (e.g., Figs. 10, 33). We have no explanation as yet for this apparent distribution of fracture orientations.

The principal purpose of constructing the deformation maps was to aid in the search for textural differences between the samples that slid stably and the ones that showed stick-slip motion. This topic is discussed in Moore et al. (1990) and will therefore be only briefly summarized here. In the low-pressure, stably sliding samples, the shear is accommodated in zones within the main fault that are as much as 1.5 mm wide and that are characterized by a marked reduction in grain size, along with the formation of numerous synthetic Riedel shears and a fabric defined by deformed, elongate micas. The slip paths for such samples are drawn as a series of elongate zones of varying thickness (e.g., Figs. 8, 9, 14, 23). In contrast, shear in the high-pressure, stick-slip samples is more highly localized along zones that are roughly 0.2 mm or less in width and that contain as many as four, 0.005 to 0.010 mm wide, subparallel shear bands consisting of extremely fine-grained gouge. In the corresponding maps of the principal slip paths, the groups of shear bands are indicated by single lines (e.g., Figs. 17, 18, 26, 27). Each shear band may represent a single episode of slip, indicating that successive slip events in the stick-slip cycle can occur as fresh breaks in the same part of the fault. Conversely, the number of slip events in a given stick-slip experiment (Figs. 2-5) is usually greater than the number of shear bands occurring together, suggesting that movement may switch to other parts of the fault, perhaps as a result of strain hardening along the earlier-formed shears. The stick-slip samples therefore show many more separate slip paths than the stably sliding samples, as indicated by the larger numbers of lines (compare, for example, Figs. 8 and 12 from Group I, or Figs. 22 and 25 from Group II).

The textural differences between the stably sliding and stick-slip samples emphasize the correlation between stick-slip and the localization of shear within fault zones. The patterns of deformation are very similar to those observed following friction experiments in which the samples contained a layer of artificial or natural gouge placed along a diagonal sawcut (e.g., Moore et al., 1986, 1988, 1989). This correspondence suggests that the deformation textures reflect the processes controlling the sliding behavior.

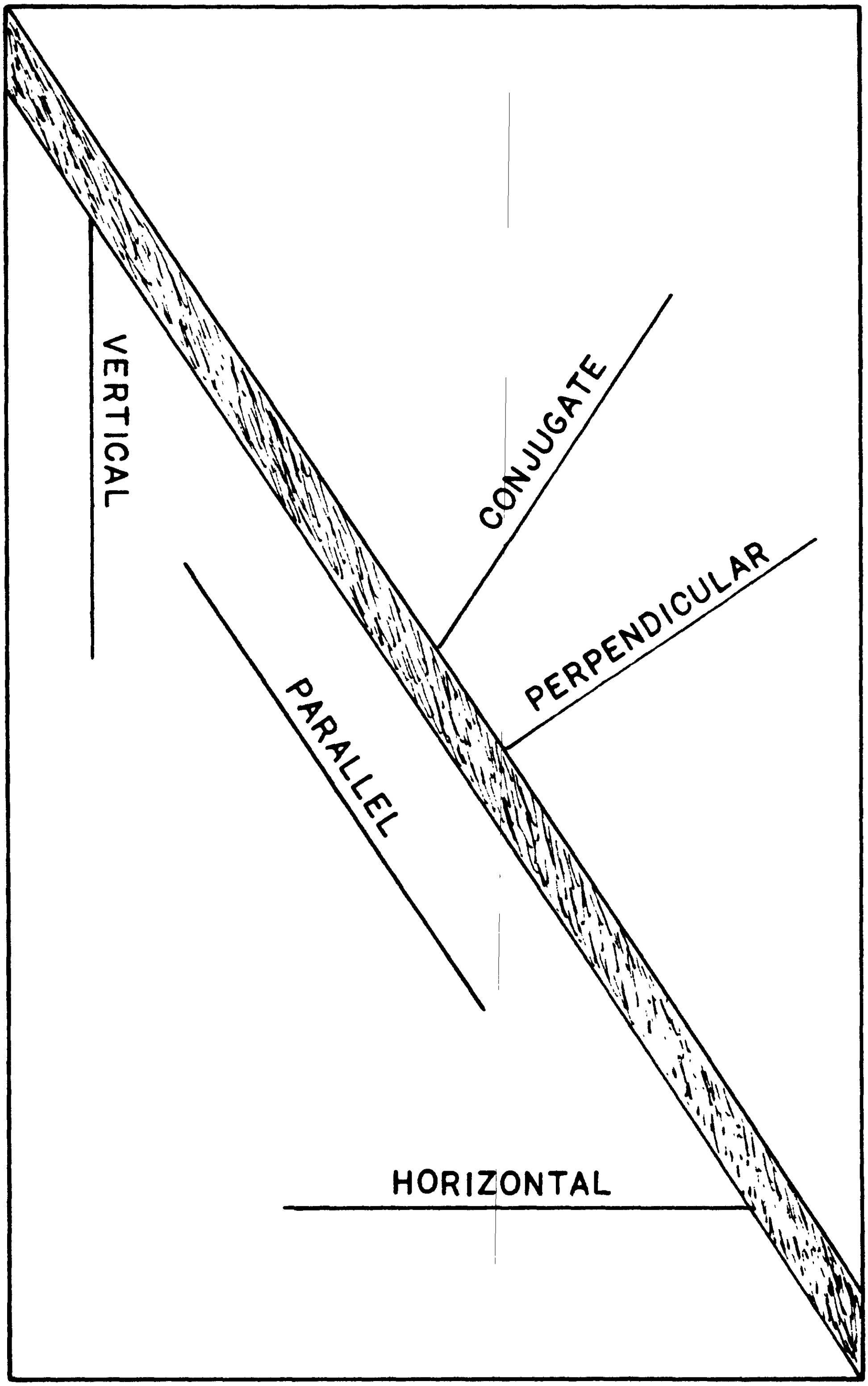

Figure 41. Principal orientations of the fractures that surround the main fault zone. The vertical and horizontal fractures are named according to their orientation in the map. The parallel, perpendicular, and conjugate faults are named according to their orientations relative to the main fault zone.

FAULT ANGLES

Examination of the deformation maps presented in the preceding section shows that the orientation of the main fault zone varies from sample to sample (compare, for example, Figs. 9 and 16, or Figs. 22 and 25). In order to look for patterns in fault orientation, the angle that the main fault makes with the axis of the granite cylinder was measured for each faulted sample. Precise determination of the angle was difficult for some samples, because of the presence of splays (e.g., Fig. 17) or bends (e.g., Fig. 34) near one end of the fault. In such cases, either an average angle, as in the case of Figure 15, or the orientation of the predominant fault segment, as in Figure 14, was chosen. The reported angles must be considered as rough estimates, but they can be useful in outlining the general trends in fault orientation.

In Figure 42, the measured fault angles are plotted relative to the confining pressures of the experiments producing the faults. With a single exception (R125), all of the values fall into a relatively wide zone in which an increase in fault angle is roughly correlated with an increase in confining pressure. A direct correlation between fault angle and confining pressure has also been described by Paterson (1958). A given confining pressure can, nevertheless, be associated with a range of fault angles, especially at the low-pressure end. The approximate boundaries of the zone in Figure 42 are indicated by dashed lines whose slopes decrease markedly at high confining pressures. This suggests the possibility of a maximum fault angle of about 40° for the granites; the largest measured angle was 38°. Faulting experiments conducted at confining pressures greater than the 621 MPa maximum of this study are required to test the possibility of a limiting value for the fault angles.

Figure 43 is a histogram of the number of faults with a given orientation. In addition, an attempt was made to separate the samples into a low-angle, low-pressure group and a high-angle, high-pressure group. The least amount of overlap between groups and the fewest anomalous values were obtained with a division made according to the sliding behavior of the samples. The resulting groups are shown in Figure 43, with the transitional Barre sample at 200 MPa (Fig. 4) included among the stick-slip samples. Indicated separately in Figure 43 are the samples from Groups II and III that were halted immediately after the initial failure. As expected, those samples that were run at 100 MPa (labelled 1 in Fig. 43) plot among the group of low-pressure, stably sliding samples, whereas those run at 500 MPa (labelled 5 in Fig. 43) plot among the high-pressure, stick-slip samples. If a causal relationship exists between fault orientation and sliding behavior, the sliding motion would necessarily be a consequence of the fault orientation, because the angle is determined prior to slip. The apparent correlation suggested by Figure 43 may be fortuitous, however, with the fault angle and sliding behavior being functions of confining pressure but not related to each other.

KINK BANDS

Kink bands can be considered as monoclinal folds with planar limbs and angular hinge zones (e.g., Verbeek, 1978). They are found in geologic structures containing a planar fabric at all scales from that of single mica crystals, through individual laminated or foliated rock units,

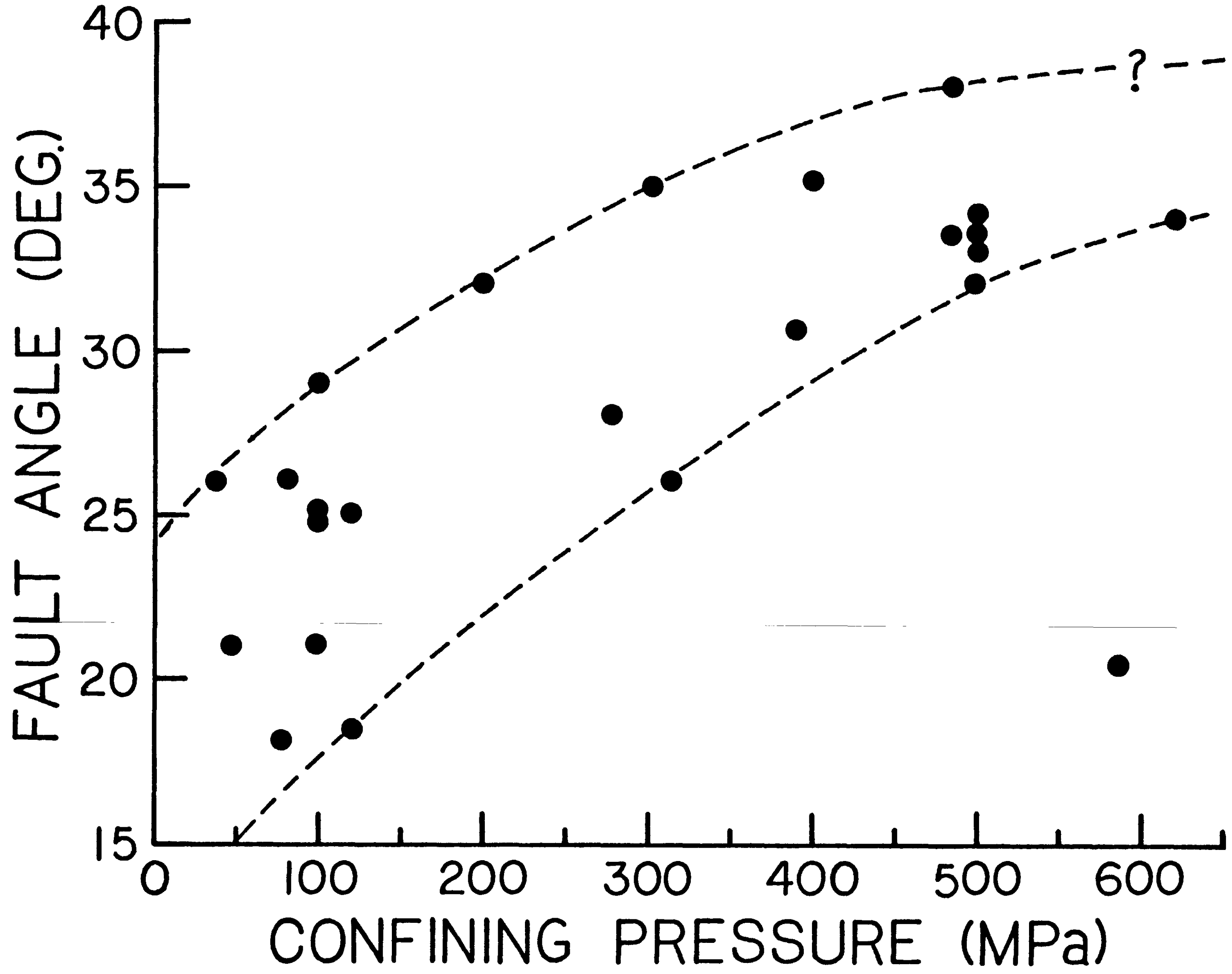

Figure 42. Plot of the angle that a given fault zone makes with the cylinder axis versus the confining pressure of the experiment producing the fault. Because of irregularities in the faults, several of the angles are average values or best fits. With one exception (sample R125), all of the points fall in a wide zone delimited by dashed lines, showing a tendency for increasing fault angle with increasing confining pressure. The data suggest a possible maximum fault angle of about 40° for the granitic rocks.

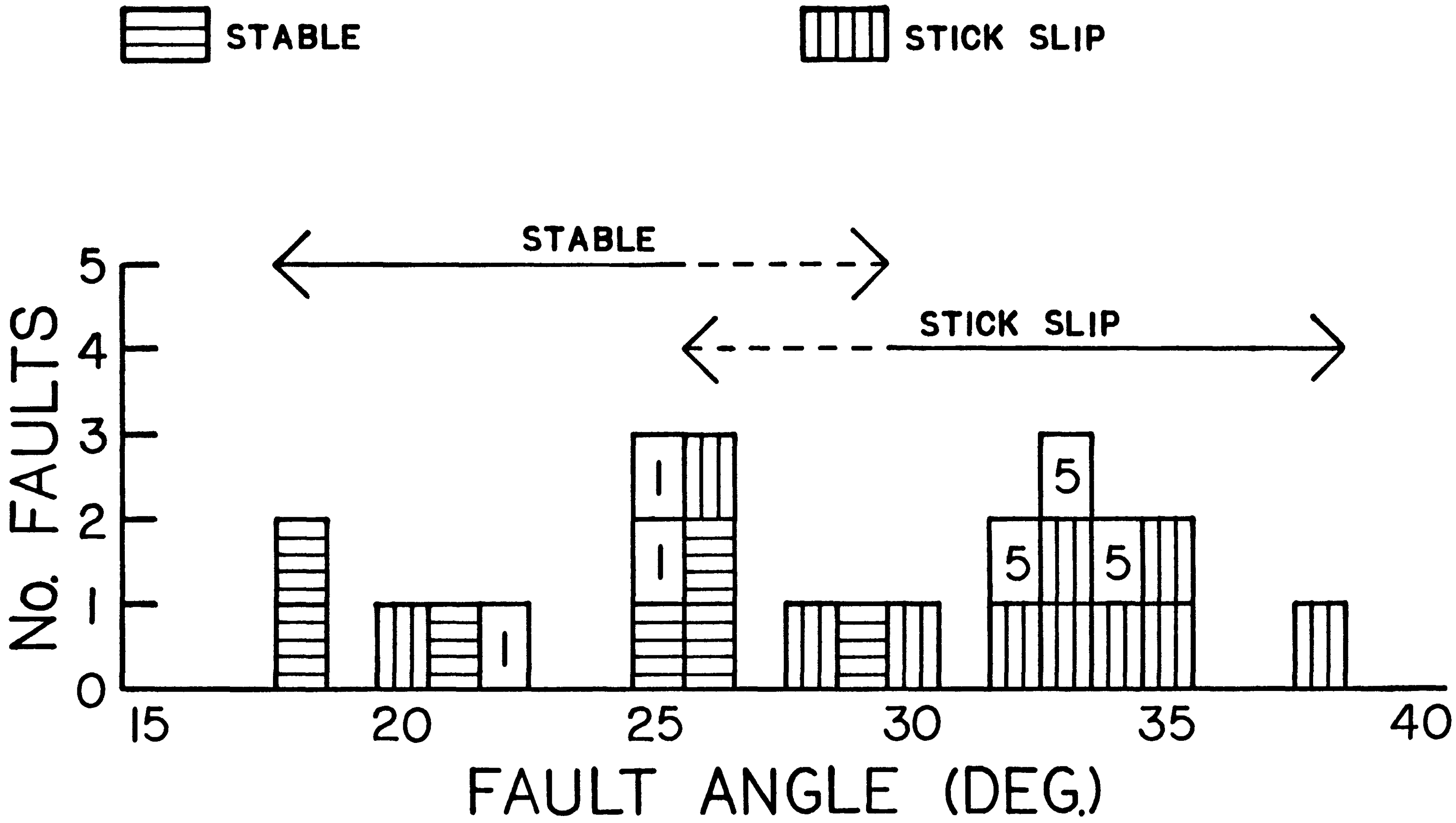

Figure 43. Histogram of fault angles, identified according to the sliding behavior of the experiment. The samples labelled 1 and 5 are from experiments that were terminated at the point of initial faulting; 1 = 100 MPa confining pressure, 5 = 500 MPa confining pressure. The samples labelled 1 plot among the low-pressure, stably sliding samples, and those labelled 5 are in the group of high-pressure, stick-slip samples.

to kilometers-thick layered sequences in mountain belts. The development of kink bands produces a shortening parallel to the original layering, in response to a major principal stress acting in that direction (Anderson, 1964).

The experimental samples examined in this study contain numerous kinked micas; two examples are shown in Figure 44. The structures range from the simple kinks shown in Figure 44a to the complex groupings of Figure 44b. Conjugate sets of kinks arranged in a zig-zag pattern along the length of the crystal are also common (see Paterson and Weiss, 1966, for photomicrographs of conjugate kinks in phyllite). As demonstrated experimentally by Paterson and Weiss (1966), kink bands are best developed when the layering (in this case the sheeted structure of the micas) is oriented at 0-10° to the compression direction, although some kinking can occur when the angle is as large as 25°.

Counts were made of the numbers of kinked crystals visible in the thin sections of the Group I and II samples. Detailed examinations of kink-band geometry were not made for this report, although such a study would be of possible future interest, to compare the observed geometry with that predicted from the various hypotheses for the development of kink bands. The total number of kinked micas in each sample was first determined, with micas containing a single kink band being given equal weight to ones having complex arrays of kinks. The total was then normalized to a standard thin-section area of 25 x 40 mm = 1000 mm^2. Examination of the starting material yielded no examples of kinked grains in Westerly but several in Barre (61 grains, when normalized to the standard area). In order to make the Westerly and Barre results directly comparable, the number of kinked grains in the Barre starting material was subtracted from the normalized total for each Group II sample.

The numbers of kinked grains obtained by this method for Westerly and Barre are plotted relative to confining pressure in Figures 45 and 46, respectively. The dashed lines delimit a marked change in the numbers of kinked micas, from smaller numbers at low confining pressures to larger numbers at higher confining pressures. The Westerly samples constrain the transition to between 277 and 313 MPa; the Barre results place the transition at the low end of this range, below 300 MPa. The increase in kinked grains occurs at a confining pressure about 100 MPa higher than that marking the change from stable to stick-slip motion (Figs. 2-5).

The numbers 67 and 90 in the Barre figure (Fig. 46) refer to those samples for which the experiment was terminated at a differential stress estimated to be 67 and 90%, respectively, of the failure stress. These data show that before the sample fails the number of kinked grains increases with increasing differential stress and axial compression. In contrast, those samples from Barre experiments terminated just after the initial break contain similar numbers of kinked grains to those from experiments with several millimeters of subsequent shear. The generation of the kinked micas in the granite cylinders may therefore be a response to compression of the sample prior to failure. The correlation between confining pressure and the number of kinked crystals may be due to the increased amount of axial compression that is experienced by the higher-pressure samples prior to failure (Figs. 2-5). After the sample fails, the strain becomes concentrated within the fault zone, so that the rest of the granite cylinder is not appreciably affected by additional strain.

Comparing the results in Figures 45 and 46, the Barre samples contain considerably larger numbers of kinked micas than corresponding Westerly samples, despite the correction made to the Barre counts for kinked crystals in the starting material. Barre does contain 14% micas by volume (biotite + muscovite + chlorite) compared to 10% in Westerly (Moore et al.,

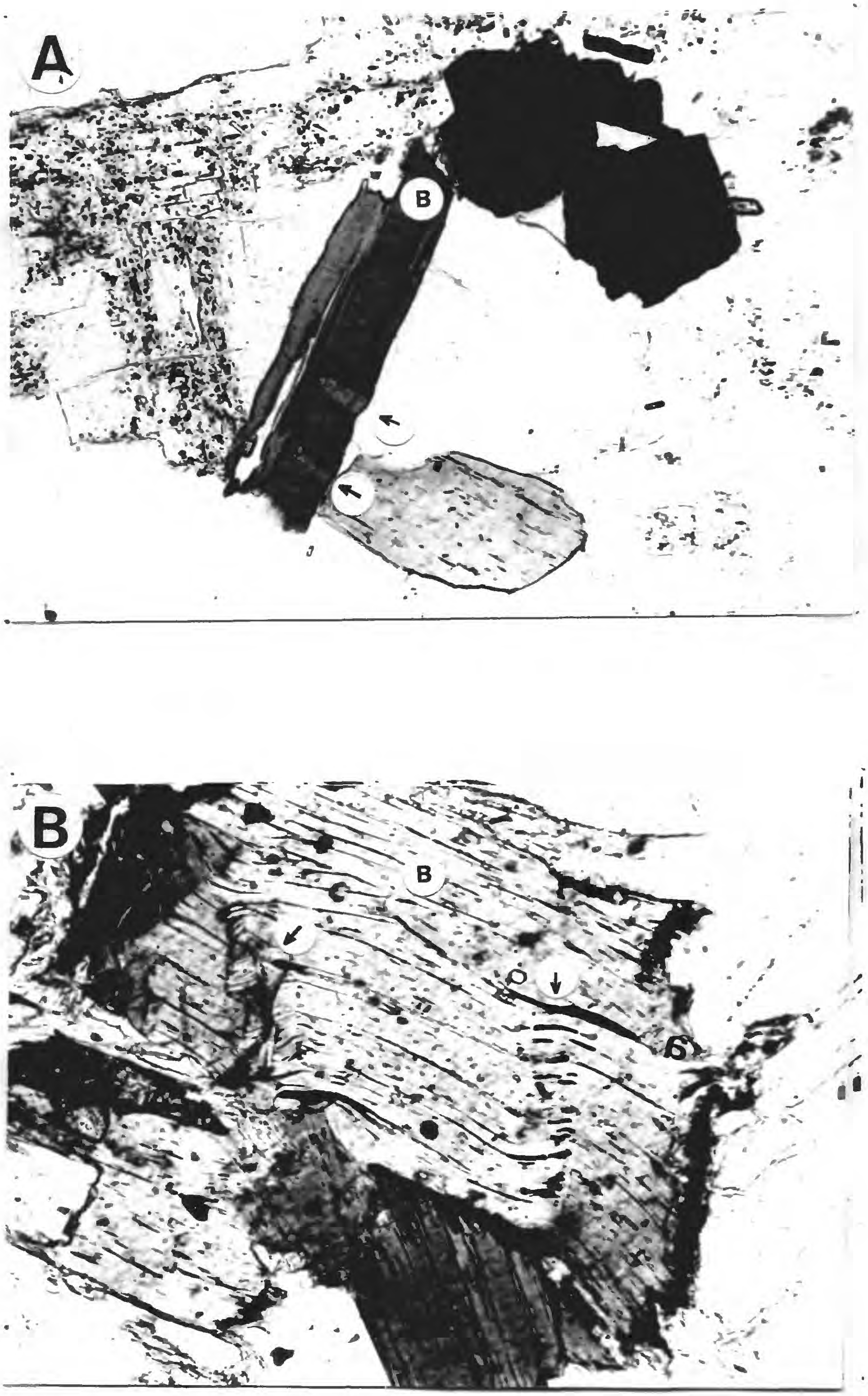

Figure 44. Examples of kinked micas from some of the experimental samples: a) a biotite from Group I Westerly sample RSW1 with two simple kink bands; b) a large biotite from Barre sample RSG5B containing complex sets of kink bands.

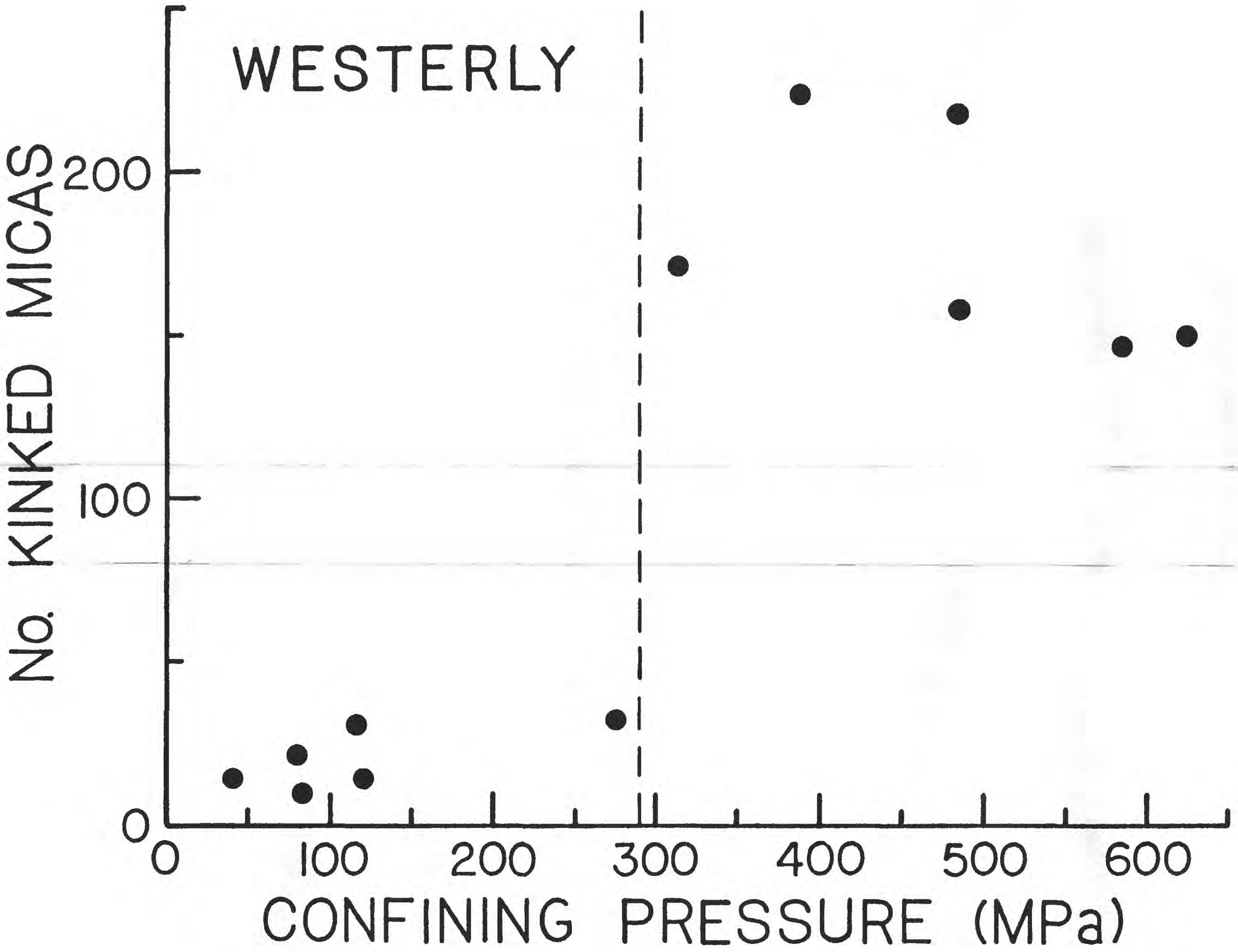

Figure 45. Counts of kinked micas in the Group I Westerly samples, plotted according to the confining pressures of the experiments. The numbers are normalized to a standard thin-section area of 1000 mm^2, but the Westerly starting material contained no kinked grains to require a correction for that. The counts show an abrupt increase at about 300 MPa confining pressure.

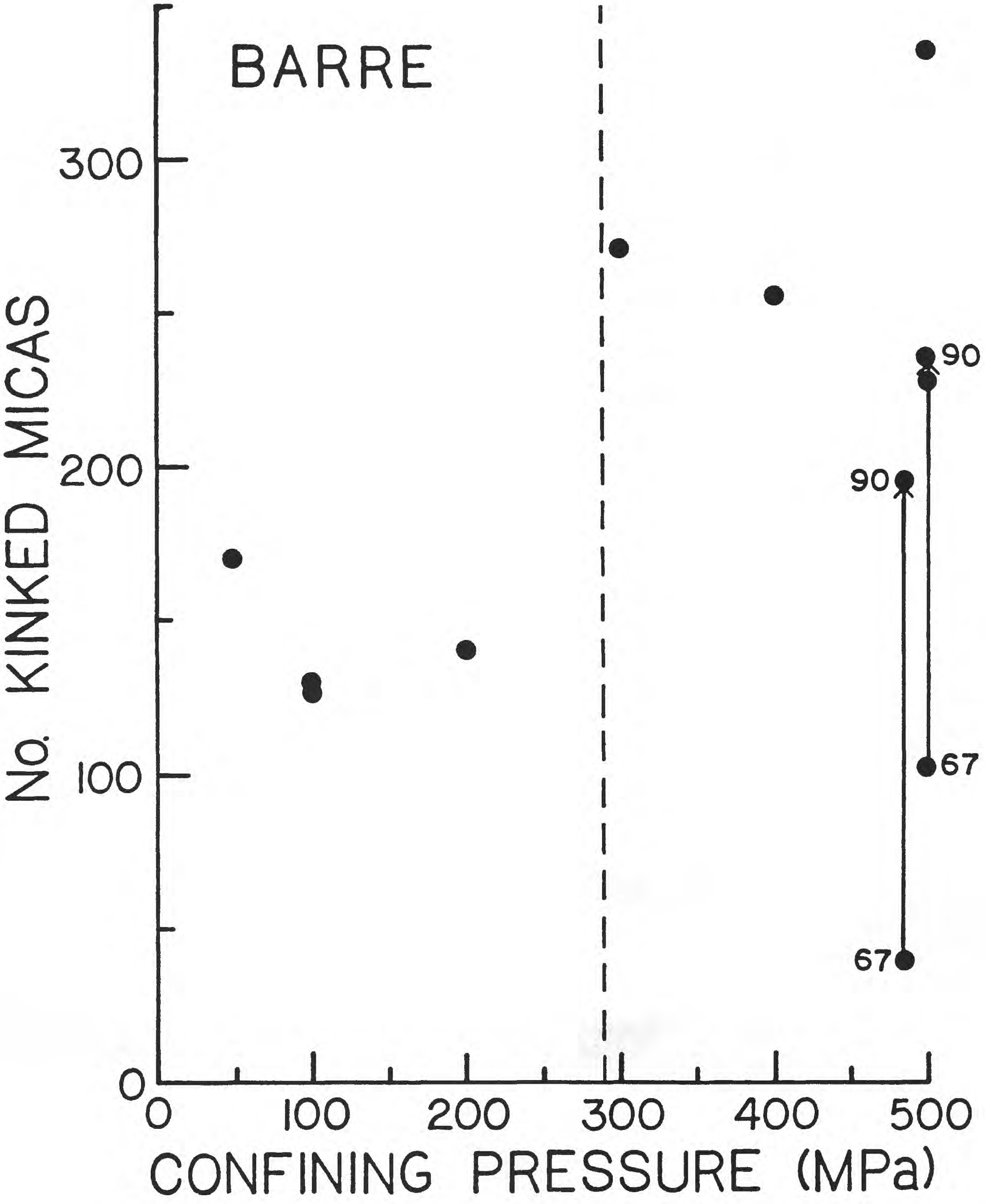

Figure 46. Counts of kinked micas in the Group II Barre samples, normalized with respect to thin-section area and corrected for the 61 kinked grains counted in the Barre control sample. The numbers 67 and 90 indicate experiments that were terminated at 67% and 90%, respectively, of the estimated failure stress at 485 and 500 MPa confining pressure. The two experiments at 485 MPa were run using room-dry cylinders; all of the others used cylinders that were pre-saturated with deionized water. The faulted samples show a marked increase in the numbers of kinked grains, starting at 300 MPa.

1987); however, the number of kinked crystals was counted rather than the volume occupied by those crystals. Because of its smaller average grain size, Westerly contains roughly 35% more mica crystals than does Barre; this percentage was obtained from counts of micas in the thin sections of the Westerly and Barre starting material. The numbers of mica grains in the two rocks cannot, therefore, be used to explain the different counts of kinked micas in Figures 45 and 46. Perhaps the larger size of the Barre micas makes them somehow more susceptible to kinking. The micas in Westerly and Barre are not obviously aligned, so that differences in the relative orientations of a foliation and the maximum principal stress (Paterson and Weiss, 1966) cannot explain the differences between Figures 45 and 46.

With the exceptions of the two samples labelled 67 and 90 at 485 MPa confining pressure, all of the Barre samples in Figure 46 were pre-saturated with deionized water (Table 1). Despite their very similar confining pressures, the two room-dry Barre samples have smaller numbers of kinked grains than the corresponding fluid-saturated samples. All of the Westerly samples plotted in Figure 45 were run under room-dry conditions, and the differences in kinked-mica counts between the room-dry Westerly and the saturated Barre samples is consistent with the differences between the pairs of unfaulted Barre samples. How the degree of filling of the pore spaces might affect the formation of kink bands is as yet unknown.

FLAME PERTHITE

Perthite is the name for an intergrowth of subordinate Na-feldspar with K-feldspar. The intergrowth can assume a variety of forms that are named according to their appearance, resulting in descriptions of patch, braid, string, film, vein, and rod perthite, among others (see Smith, 1974, Chapter 19, for a review article on perthite). "Flame" perthite (Smithson, 1963), which is also referred to in some papers as "plume" perthite (e.g., Alling, 1932; Gates, 1953), refers to an irregular form of perthite in which the sodic plagioclase has a feathery or flame-like appearance; two examples of K-feldspar crystals from Barre granite that contain flame perthite are shown in Figure 47. The flames generally occur in clusters that coalesce and terminate at the edge of the K-feldspar crystal or along a fracture within it.

The origin of perthite is not fully understood, but most theories are tied to either exsolution or replacement processes (see review in Smith, 1974). Specific forms of perthite may commonly be linked to a specific origin; for example, thin, regularly spaced film perthite is generally considered to form by exsolution of Na- from K-feldspar, whereas coarse patch perthite is usually attributed to replacement of K-feldspar by albite. Exsolution (e.g., Goldich and Kinser, 1939; Gates, 1953) or replacement (Smith, 1974) as a result of differential stress is commonly invoked as causing the formation of flame perthite. The differential stress may provide the energy needed to promote the unmixing of the Na- and K-components of alkali feldspar, which would otherwise remain as a metastable solid solution (e.g., Chayes, 1952); the unmixed Na component would then migrate to areas of lower stress along fractures or grain boundaries (Gates, 1953). If this hypothesis for the origin of flame perthite has merit, then the loading of the granite cylinders during the intact-rock experiments could potentially promote the development of flame perthite in K-feldspar, at least if the rate of formation is sufficiently rapid under the experimental conditions tested.

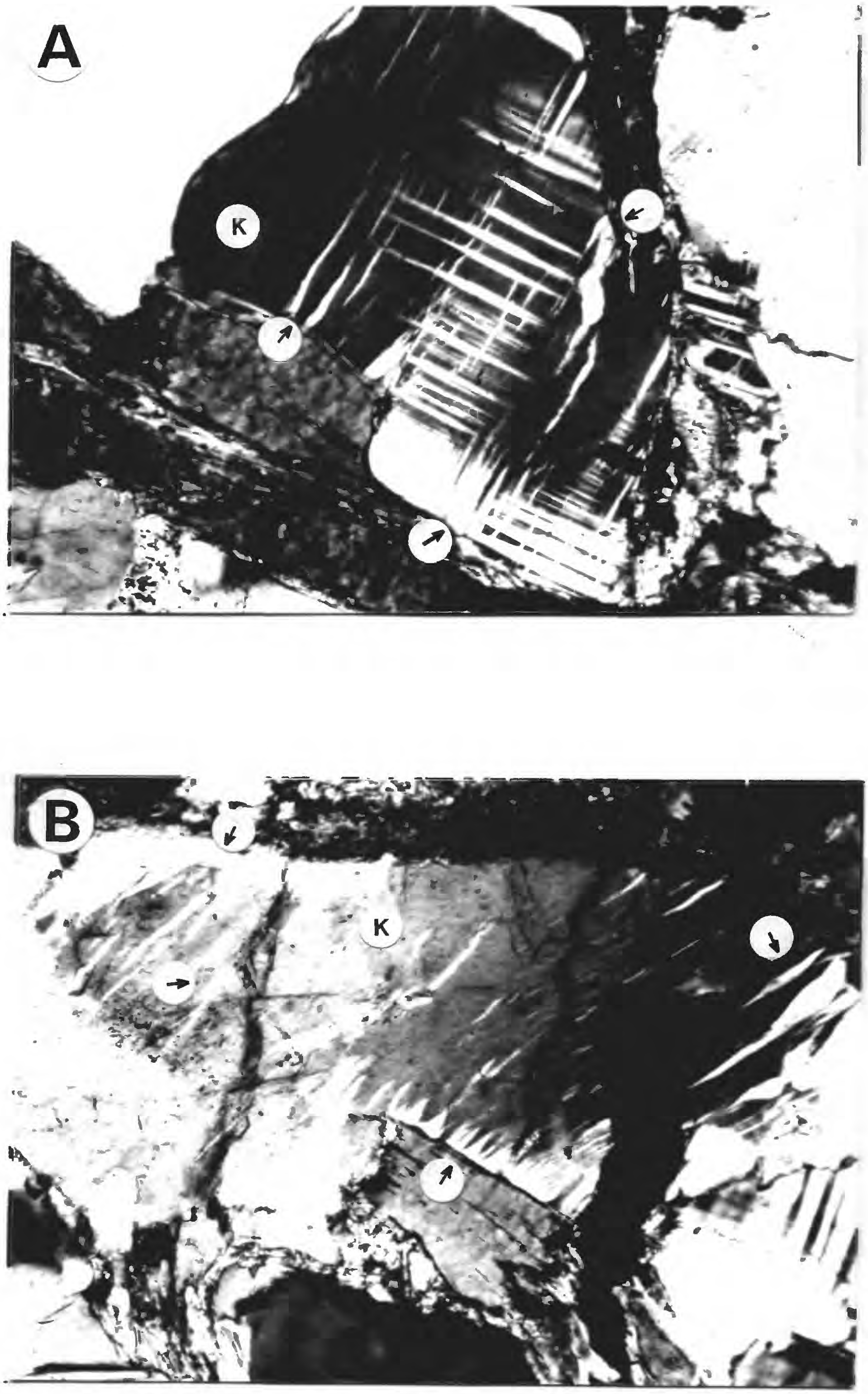

Figure 47. Examples of flame perthite in K-feldspar crystals from Group II Barre samples: a) RSG4B; b) RSG9B. The flame perthites occur as irregular, wavy forms extending into the K-feldspar crystals from the edges. One set in b) terminates at a fracture that cuts across the crystal. Where best developed, the albite of the flame perthite stands out because of its slightly higher birefringence (low second order) compared to the host K-feldspar.

Counts of flame perthite in the Group II samples were made, because some of the faulted Barre samples appeared to contain unusually large numbers of well-defined flame perthite, several examples being associated with fractures. The faulted Westerly samples seemed to contain only a few, relatively faint examples of flame perthite; nevertheless, the Group III Westerly samples were counted, to compare with the Barre results. The counts for Barre and Westerly are shown in Figures 48 and 49, respectively. Adjustments for thin-section area and for flame perthites in the starting material (42 grains) were made for the Barre results in Figure 48, similar to the corrections for the counts of kinked micas. An area correction only was made for the Westerly results in Figure 49, and the area-corrected count for the starting material (29 grains) is included in the figure.

The Barre thin sections (Fig. 48) show a significant rise in the numbers of flame perthite over the starting material. At a given confining pressure, the numbers increase as the differential stress and axial compression increase prior to sample failure. Most of the Group III Westerly samples contain a few more flame-perthite-bearing feldspars than the 29 grains of the starting material (Fig. 49), but this increase is about an order of magnitude smaller than that for Barre (Fig. 48). No obvious relationship was found between confining pressure and the counts for either rock type.

The results in Figure 48 and, to a lesser extent, Figure 49 are consistent with the generation of flame perthite in the granite cylinders as a result of the imposition of a differential stress. As was the case with the kinked micas, the Barre samples were much more affected than the Westerly samples. The relative compositions of the K-feldspars in the two granites cannot explain their different flame perthite counts, because the K-feldspars in Westerly have higher Na contents, at 0.8 wt % Na_2O, than those in Barre, which contain 0.6 wt % Na_2O (Moore et al., 1983, 1987). One possible explanation for the difference may be that the strained Barre feldspars exsolve more readily than the undeformed Westerly ones because of their higher lattice energy. This topic deserves more thorough treatment, because of the possible generation of chemical/mineralogical adjustments through the application of a differential stress in laboratory experiments.

SUMMARY

Faulting and shearing experiments were conducted at room temperature on cylinders of Westerly and Barre granite. Thin sections of the samples were examined and maps prepared of the fracture patterns and shear paths, with the following purposes: (1) to determine the extent and types of deformation that precede sample failure; (2) to study the overall characteristics of faulting in the samples; and (3) to look for differences between the deformation patterns of stick slip and stably sliding samples.

Several types of deformation feature appear in the granite cylinders prior to sample failure. The amount of microfracturing increases with increasing axial compression in the unfaulted samples; but even samples taken to 99% of the failure stress give no indication of the eventual site of faulting. The development of kink bands in mica and of flame perthite in K-feldspar is also linked to the application of a differential stress/axial compression prior to sample failure. Even allowing for natural strain features in the starting material, the Barre samples acquire many more kinked micas and flame perthites during the experiments than do the

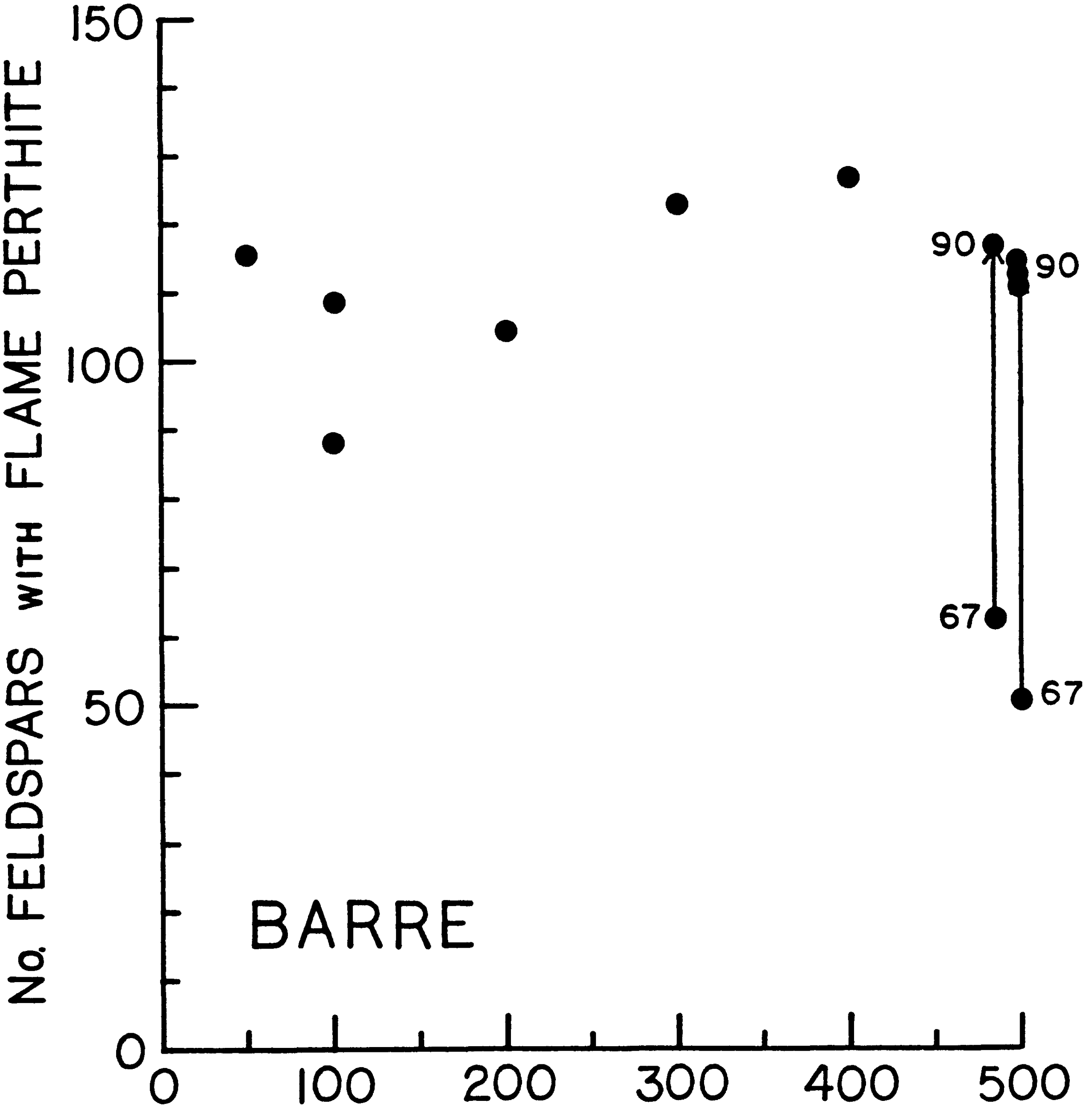

Figure 48. Counts of K-feldspar crystals containing flame perthite in the Group II Barre samples. Corrections for thin-section area and for flame perthite in the starting material were made, as in Figure 46. The numbers 67 and 90 refer to the same samples as described in Figure 46. There is a significant increase in the numbers of flame perthites in the faulted samples, but no relation to confining pressure was found similar to that observed with the counts of kinked micas. The numbers do increase with increasing differential stress and/or axial compression prior to faulting.

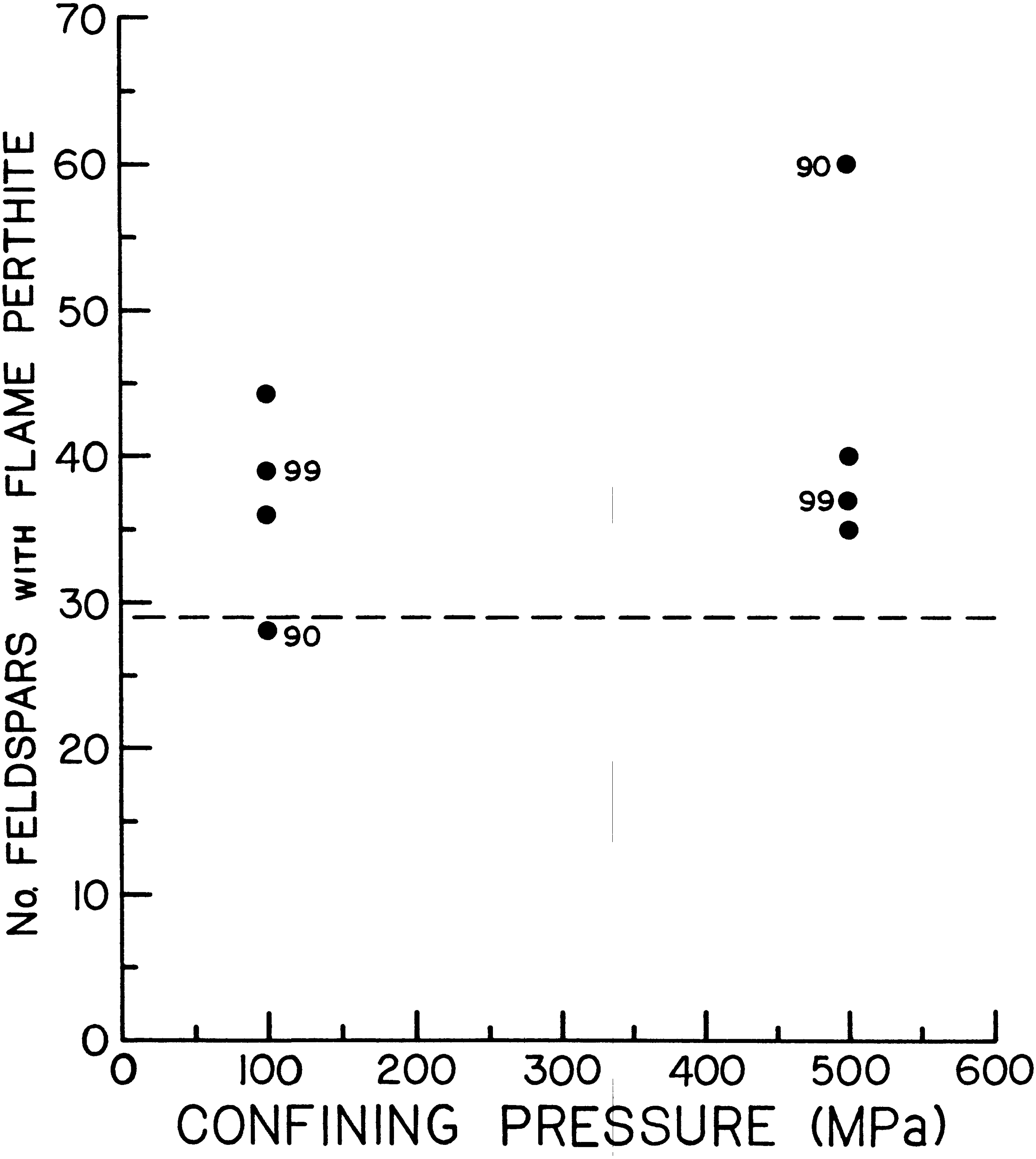

Figure 49. Counts of K-feldspar crystals containing flame perthite in the Group III Westerly samples. Corrections for thin-section area only were made, as in Figure 45. The count of flame perthites in the control sample (29 grains) is drawn as a dashed line across the figure. Most of the samples show a slight increase in the numbers of flame perthites over the starting material, but the counts are significantly lower than those in Figure 48.

Westerly samples. Following sample failure, deformation is concentrated along the main fault, and the surrounding granite cylinders show no additional increases in the numbers of these deformation features.

The samples that were loaded beyond the failure point characteristically contain a principal fault surrounded by a zone of fracturing. The orientation of the main fault can be roughly correlated with the confining pressure of the experiment. Faults developed during low-pressure experiments generally make a smaller angle to the axis of the granite cylinder than those developed in the high-pressure experiments. The fractures surrounding the main fault can be roughly separated into 5 groups, according to their orientation. Some of these groups are equally distributed among the samples, whereas others occur preferentially in samples from low-, intermediate-, or high-pressure experiments. The reason for the preferential distribution of some fractures is unknown.

The paths of concentrated shear in the samples were identified by the presence of deformation features such as offset minerals, grain-size reduction, a mineral fabric, or secondary shear bands. Shear in the stick-slip samples was highly localized to zones 0.2 mm or less in width, which in turn consist of one or more shear bands of extremely fine-grained gouge. In contrast, shear in the stably sliding samples occurred in zones that were up to 1.5 mm in thickness, and the predominant deformation feature was a mineral fabric. The textural differences between these stably sliding and stick-slip samples have also been observed in analogous samples containing a layer of natural or artificial gouge placed along a sawcut surface. This correspondence suggests that the same controls on sliding behavior are operative, whatever the nature of the starting material.

REFERENCES

Alling, H.L., 1932. Perthites. American Mineralogist 17: 43-65.

Anderson, T.B., 1964. Kink-bands and related geological structures. Nature 202: 272-274.

Chayes, F., 1952. On the association of perthitic microcline with highly undulant or granular quartz in some calcalkaline granites. American Journal of Science 250: 281-296.

Gates, R.M., 1953. Petrogenetic significance of perthite. Geological Society of America Memoir 52: 55-69.

Goldich, S.S., and Kinser, J.H., 1939. Perthite from Tory Hill, Ontario. American Mineralogist 24: 407-427.

Moore, D.E., Morrow, C.A., and Byerlee, J.D., 1983. Chemical reactions accompanying fluid flow through granite held in a temperature gradient. Geochimica et Cosmochimica Acta 47: 445-453.

Moore, D.E., Morrow, C.A., and Byerlee, J., 1987. Fluid-rock interaction and fracture development in 'crystalline' rock types. U.S.G.S. Open-File Report 87-279: 53 p.

Moore, D.E., Summers, R., and Byerlee, J.D., 1986. The effects of sliding velocity on the frictional and physical properties of heated fault gouge. Pure and Applied Geophysics 124: 31-52.

Moore, D.E., Summers, R., and Byerlee, J.D., 1988. Relationship between textures and sliding motion of experimentally deformed fault gouge: Application to fault zone behavior. Proceedings of the 29th U.S. Symposium on Rock Mechanics: 103-110.

Moore, D.E., Summers, R., and Byerlee, J.D., 1989. Sliding behavior and deformation textures of heated illite gouge. Journal of Structural Geology 11: 329-342.

Moore, D.E., Summers, R., and Byerlee, J.D., 1990. Deformation of granite during triaxial friction tests. Proceedings of International Conference on Mechanics of Jointed and Faulted Rock; April 18-20, 1990; Vienna, Austria.

Paterson, M.S., 1958. Experimental deformation and faulting in Wombeyan marble. Geological Society of America Bulletin 69: 465-476.

Paterson, M.S., and Weiss, L.E., 1966. Experimental deformation and folding in phyllite. Geological Society of America Bulletin 77: 343-374.

Smith, J.V., 1974. Feldspar Minerals. Springer Verlag: New York. Volume II, Chapter 19, pp. 399-519.

Smithson, S.B., 1963. Granite Studies. II. The Precambrian Fla granite, a geological and geophysical investigation. Norges Geologiske Undersokelse 219: 212 p.

Summers, R., and Byerlee, J., 1977. Summary of results of frictional sliding behavior, at confining pressures up to 6.98 kb, in selected rock materials. U.S.G.S. Open-File Report 77-142: 129 p.

Verbeek, E.R., 1978. Kink bands in the Somport slates, west-central Pyrenees, France and Spain. Geological Society of America Bulletin 89: 814-824.